Doppler lidar measurements of wind variability and LLJ Properties in Central Oklahoma during the August 2017 Land-Atmosphere Feedback Experiment.

Yelena L. Pichugina[a, b], Robert M. Banta[a, b], W.Alan Brewer[b], D.D. Turner[c], V.O. Wulfmeyer[d], E.J. Strobach[a, b], S. Baidar[a, b], and B.J. Carroll[a, b]

[a]*CIRES, University of Colorado, Boulder, CO, USA*

[b]*NOAA Chemical Sciences Laboratory, Boulder, CO, USA*

[c]*NOAA Global Systems Laboratory, Boulder, CO, USA*

[d]*University of Hohenheim, Germany*

Corresponding author: Yelena Pichugina, Yelena.Pichugina@noaa.gov

File generated with AMS Word template 2.0

Early Online Release: This preliminary version has been accepted for publication in *Journal of Applied Meteorology and Climatology*, may be fully cited, and has been assigned DOI 10.1175/JAMC-D-22-0128.1. The final typeset copyedited article will replace the EOR at the above DOI when it is published.

ABSTRACT

Low-level jets (LLJs) are an important nocturnal source of wind energy in the U.S. Great Plains. An August 2017 lidar-based field-measurement campaign (LAFE) studied LLJs over the Central SGP site in Oklahoma, and found nearly equal occurrences of the usual southerly jets, and postfrontal northeasterly jets—typically rare during this season—for an opportunity to compare the two types of LLJs during this month. Southerly winds were stronger than the north-easterlies by more than 4 ms^{-1} on average, reflecting a significantly higher frequency of winds stronger than 12 ms^{-1}.

The analysis of this dataset has been expanded to other SGP Doppler-lidar sites to quantify the variability of winds and LLJ properties between sites of different land use. Geographic variations of winds over the study area were noted: on southerly-wind nights, the winds blew stronger at the highest, westernmost sites by 2 ms^{-1}, whereas on the northeasterly-flow nights, the easternmost sites had the strongest wind speeds. Lidar measurements at 5 sites during August 2017, contrasted to the 2016-2021 summertime data, revealed unusual wind and LLJ conditions.

Temporal hodographs using hourly-averaged winds at multiple heights revealed unorganized behavior in the turbulent stable boundary layer (SBL) below the jet nose. Above the nose, some nights showed veering qualitatively similar to inertial-oscillation (IO) behavior, but at amplitudes much smaller than expected for an IO, whereas other nights showed little veering. Vertical hodographs had a linear shape in the SBL, indicating little directional shear there, and veering above, resulting in a hook-shaped hodograph with height.

SIGNIFICANCE STATEMENT

Doppler-lidar measurements at the Atmospheric Radiation Measurement (ARM) Southern Great Plains (SGP) were used to quantify the variability of winds and low-level jet (LLJ) properties between five sites of different land use and wind regimes across this area.

Knowledge of wind and LLJ structure and dynamics is important for many applications, and strong southerly LLJ winds at night are an important resource for wind energy.

The analysis of multi-year (2016-2021) summertime LLJ parameters provided insight into the LLJ climatology in this part of the Great Plains.

Accepted for publication in *Journal of Applied Meteorology and Climatology*. DOI 10.1175/JAMC-D-22-0128.1.

1. Introduction

The southerly, nocturnal, warm-season low-level jet (LLJ) of the US Great Plains has been widely studied for decades because of its importance in many applications. Its role in transporting moisture northward from the Gulf of Mexico, thus contributing significantly to severe weather and precipitation during the agricultural season, has been well documented (e.g., Means 1954, 1954; Pitchford and London 1962; Mo et al. 1995; Higgins et al. 1997; Mitchell et al. 1997; Song et al. 2005; Pu et al. 2014; Gebauer et al. 2018; Smith et al. 2019; Carroll et al. 2021). LLJs have also been shown to be efficient in transporting urban-generated pollutants away from urban centers at night (Banta et al. 1998, 2005; Klein et al. 2014). More recently wind energy has become an important application for meteorological information, and strong southerly LLJ winds at night can be an important resource for wind turbine operations.

These and other applications require accurate forecasts of LLJ properties as well as knowledge of long-term mean geographical distributions and variations of LLJ properties in the horizontal. For wind energy, quantitative wind information is needed for atmospheric layers above the surface occupied by the wind-turbine rotor blades (*rotor layer*) and such information would be most beneficial at accuracies of 0.1 m s^{-1} or better (Banta et al. 2013). The rotor layer of current land-based wind turbines generally extends somewhere between 40 and 150 m AGL or higher, where wind characteristics during LLJ conditions often differ significantly from those near the surface (Banta et al. 2013, 2018). Thus, quantitative characteristics of the vertical profile of the wind and turbulence below 200 m are of prime importance to wind energy, but profiles up to several hundreds of meters AGL are also needed to provide meteorological context. The variability of winds across wind farms, which may be 50-100 km or more across, under different conditions, is also of interest.

Several mechanisms have been proposed to explain evening LLJ accelerations in the Great Plains. The late-afternoon/early-evening surface cooling and consequent decoupling of the flow above the surface from surface friction, which disrupts the daytime balance of forces and leads to ageostrophic accelerations and inertial oscillations of the flow aloft in the former convective boundary layer, was described by Blackadar (1957). Diurnal heating and cooling of the gradual east-west slope of the Great Plains, which generates diurnally varying pressure gradients and geostrophic wind cycles over the region, was proposed by Holton (1967). Using information from NAM model runs, Parish and Oolman (2010) found that the strong heating differential, between the lower, cooler, moister regions of the eastern Great Plains and the

Accepted for publication in *Journal of Applied Meteorology and Climatology*. DOI 10.1175/JAMC-D-22-0128.1.

higher, drier, hotter landscapes to the west, leads to a northerly thermal wind, resulting in the strongest southerly wind speeds near the surface, decreasing with height. The strength of LLJs was related to the magnitude of this east-west temperature differential. Understanding the relative effectiveness of each of the relevant mechanisms in producing the LLJ depends on understanding the nature of the evening decoupling processes, i.e., the magnitude and evolution of the structure of the turbulent mixing profile in the nighttime stable boundary layer (SBL).

It is likely that more than one mechanism act in concert to generate the Great Plains LLJ, which sometimes produces multiple maxima in the wind-speed profile (Banta et al. 2002, Shapiro et al. 2016). Theoretical and numerical studies have addressed the relative contributions of the Blackadar vs. the Holton vs. thermal-wind mechanisms (Zhong et al. 1996; Shapiro et al. 2016; Fedorovich et al. 2017; Parish 2017). Shapiro and Fedorovich (2009, 2010) derived and solved a set of analytic equations for vertical profiles that included both decoupling and slope physics, and found that both effects together could reproduce many aspects of the Great-Plains LLJ structure and behavior. Many NWP modeling studies have generated LLJs that peaked above 400 m, which we will refer to as *deep LLJs* (e.g., Zhong et al. 1996; Smith et al. 2018).

NWP forecast models are important tools for providing wind forecasts, and in a companion paper we investigate the ability of the NOAA's High Resolution Rapid Refresh (HRRR) model to represent LLJs. LLJ properties have not been well represented in models; for example, the maximum or nose in the wind profile has been too high, and either too weak (Storm et al. 2009*)* or too strong (Werth et al. 2011) in many attempts to simulate it. In a case-study simulation, Parish and Clark (2017) reported a jet at about the right height, but the corresponding speeds were too weak by several m s^{-1}, and Mirocha et al. (2016) noted that "significant discrepancies occurred at various times for all of the simulations in relation to the observations," within the sub-jet layer in their WRF LLJ runs. These errors have been blamed on the inadequate representation of sub-resolution-scale mixing processes, which are key to the development of LLJs during the evening transition (Mahrt 1998; Banta et al. 2003; Shapiro et al. 2016). Improvements in modeling LLJs depend on being able to accurately simulate the processes that generate them, including mixing processes in the SBL beneath the LLJ nose.

Studies during the Cooperative Atmosphere-Surface Exchange Studies (CASES-99) October 1999 field program in southeast Kansas (Poulos et al. 2002), and the Lamar Low-Level Jet Program of September 2003 (LLLJP-03; Kelley et al. 2004), were focused on SBL

Accepted for publication in *Journal of Applied Meteorology and Climatology*. DOI 10.1175/JAMC-D-22-0128.1.

properties and processes, and thus addressed the relationship between the LLJ and SBL turbulence (Banta et al. 2003, 2006, 2007; Pichugina et al. 2008, 2010). Analyses of these datasets showed modest veering in time from southeast to south-southwest through the sub-jet layer during the first 2-3 h after sunset, then little direction change for the rest of the night on most nights (Pichugina and Banta 2010). These results agreed with Lundquist (2003), who found no evidence for inertial oscillations, except for a post-frontal-passage below 1000 m AGL during CASES-99 using 915-MHz profiler data, and Vanderwende et al. (2015), who also found modest LLJ veering in time ($3° \ h^{-1}$). The absence of fully developed inertial oscillations would indicate that other processes in addition to the mechanism proposed by Blackadar must also be important in generating and maintaining the LLJ.

The existence of northerly jets is another issue addressed in LLJ studies. Whiteman (1997), Song et al. (2005), and Carroll et al. (2019) found that these were most often post-cold frontal, and Gebauer et al. (2017) studied these using the Shapiro-Fedorovich (2009) analytical model. In a typical summer, LLJs are mostly southerly, and northerly jets are infrequent (e.g., Carroll et al. 2019). In the present study, we focus on an intensive measurement campaign during August 2017, a month that saw an anomalously high incidence of cold fronts and jets having northerly- or northeasterly-component winds (Song et al. 2005).

August 2017 was the period of deployment of the Land-Atmosphere Feedback Experiment (LAFE; Wulfmeyer et al. 2018). Although primarily a daytime project, here we use this dataset, along with the longer-term network of five scanning Doppler lidars (DLIDs) at the Atmospheric Radiation Measurement (ARM) Southern Great Plains (SGP) atmospheric observatory, to characterize LLJ properties through the first 1 km AGL during the LAFE period. We compare these properties among sites, to estimate the influence of the different surface types on the magnitude of variations of winds and LLJ parameters, and we use the longer-term 2016-2021 dataset to put this month into perspective. We compare aspects of the LLJ for this period and location with findings from previous studies and construct temporal and vertical hodographs to gain insight into the structure and dynamics of the observed LLJs.

The present paper is organized as follows: Section 2 provides information on the ARM research sites and instruments used for long-term and LAFE periods, including vertical and temporal resolution of wind and turbulence data from DLIDs at all sites that are important for the interpretation of the results. Section 3 describes wind flow conditions through a deep layer at the five SGP lidar sites over six summers (2016-2021) and contrasts these findings with

Accepted for publication in *Journal of Applied Meteorology and Climatology*. DOI 10.1175/JAMC-D-22-0128.1.

those observed during the LAFE experiment in August 2017. Section 4 focuses on measured LLJ properties, their relationship to the layer mean properties from Section 3, the variability of LLJ characteristics among ARM DLID sites, and the evolution of nocturnal LLJ properties. Temporal and vertical hodographs for all five sites show similarities and differences in how these hodographs evolve at the different sites.-The main results are summarized in Section 6.

2. Background, Research area, and Doppler lidar measurements

2.1 ARM SGP lidars

ARM SGP Doppler lidars are located at the well-instrumented central facility (C1) near Lamont, Oklahoma, and the four extended facilities E32, E37, E39, and E41. The sites are separated by 56-77 km and have different surface and vegetation types from cropland to grassland and pasture (Fig.1a, Tab. 1). Wind turbines around SGP sites were deployed farm-by-farm over the years of lidar data collection. Project names and the beginning of wind-farm operations are provided on Fig. 1b.

These lidars are Halo Photonics Stream Line scanning systems and had been in continuous operation since 2010 at C1, and from 2016 at the four extended facilities. These lidars provided multi-year profile data with temporal resolution of 15-min at C1 and 10-min at E32-E41, and a vertical resolution of 24 m (C1) and 26 m (E32-E41) for wind, and 5-min, and 30 m for *w*-turbulence profiles, respectively, from 90 m above ground level (AGL) up to ~1.5 km aloft. Details of the deployment history, raw and processed data description, along with other valuable information and sample plots can be found in the Doppler lidar handbook (Newsom and Krishnamurty, 2020). Lidar datasets at all 5 sites can be found at https://www.arm.gov/capabilities/observatories/sgp.

Accepted for publication in *Journal of Applied Meteorology and Climatology*. DOI 10.1175/JAMC-D-22-0128.1.

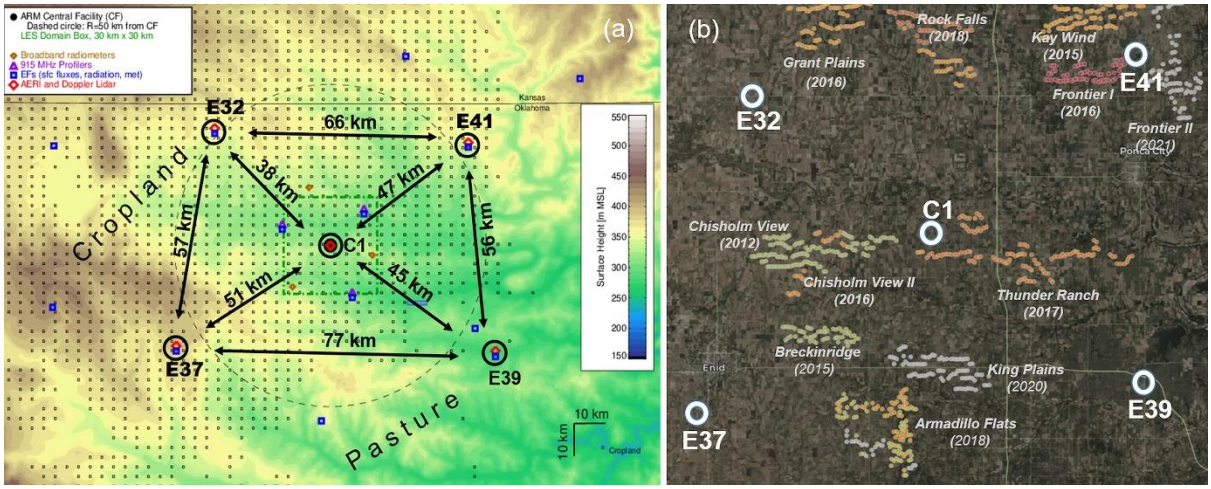

Fig. 1. (a) Location of Halo Streamline HR Doppler Lidars at the ARM Climate Research SGP Facility (black circles) superimposed on the surface elevation map of the region from a 750-m resolution HRRR simulation. Distances between the ARM central facility (C1) near Lamont and at the four extended facilities near Medford (E32), Waukomis (E37), Morrison (E39), and Peckham (E41) are indicated by black arrows. Small black squares indicate the horizontal grid points of the 3-km operational HRRR model where the primary land use type is cropland; locations with no small black squares have a primary land use type of pasture. (Figure 1 is adapted from Wulfmeyer et al, 2018). (b) Google map of wind farms around SGP site provides names of wind psis given alon. The colors indicate wind turbines of different capacities and owners (https://eerscmap.usgs.gov), and the beginning of wind farm operations is given in parenthesis.

Facility Name	Facility Code	Elevation (m)	Lat/Lon	Surface Type	Vegetation type	Start day
Central Facility, Lamont, OK	C1	318 m	36.605 N 97.485 W	Rangeland (Sandy)	12.0	2010-10-22
Medford, OK (Extended)	E32	328 m	36.819 N 97.819 W	Pasture	11.9	2016-05-03
Waukomis, OK (Extended)	E37	379 m	36.311 N 97.928 W	Cultivated field to the south, site in grass	11.9	2016-05-03
Morrison, OK (Extended)	E39	279 m	36.374 N 97.069 W	Cultivated field to the south, site in a pasture	10.0	2016-04-01
Peckham, OK (Extended)	E41	340 m	36.879N 97.086 W	Cultivated field to the south, site in a grassy field	10.0	2016-05-03

Table 1. ARM Southern Great Plains facilities with Doppler Lidar measurements

Accepted for publication in *Journal of Applied Meteorology and Climatology*. DOI 10.1175/JAMC-D-22-0128.1.

2.2. LAFE instrumentation

A large array of additional instrumentation was deployed to site C1 during the Land-Atmosphere Feedback Experiment (LAFE) in July-September 2017 (Wulfmeyer et al., 2018 BAMS, Meyers et al., 2018, Turner et al., 2017), to investigate interactions between different land-surface types and the overlying atmosphere. Key instrumentation participating in LAFE, including the various types of scanning lidars, quantities measured, as well as scientific objectives of LAFE, is summarized in Wulfmeyer et al (2018). Many of the instruments provided data continuously, but some, such as the Raman lidar, were operated in modes that optimized sampling of the lower daytime convective boundary layer. The complete list of all instruments deployed to the Central facility (C1) during the LAFE campaign can be found in Wulfmeyer et al. (2018).

2.3. Doppler lidars: wind and turbulence profiles

This paper focuses on the analysis of nighttime wind fields and LLJ characteristics obtained from the SGP Doppler lidar (SLID) long-term datasets at 5 sites and from the University of Hohenheim (UHOH) Doppler lidar (ULID) that operated during 13-31 Aug 2017 from C1. For this period the SLID measurements at C1 were switched to the vertical staring mode.

The ULID performed a continuous pattern of measurements referred to as ”6-beam scans,” a 6-beam configuration whose sampling rate is 1-Hz and whose respective azimuthal angles are 0, 60, 120, 180, 240, and 300, oriented at 45 degrees from zenith. These data were processed to derive profiles of the horizontal wind speed and direction with a temporal resolution of ~1 min and vertical resolution of 26 m, also providing computed profiles of u and v wind components and their uncertainties. The “6-beam” measurement technique allowed the computation of profiles of TKE, horizontal momentum, and variances of wind vector components, using the methods suggested by Sathe et al. (2015) and evaluated in Bonin et al. (2017).

Variables available from ULID during LAFE and the routine long-term SLID measurements are given in Appendix A (Table A). This table also provides the temporal and vertical resolution of all profiles, and the minimum available (and plotted) profile heights.

Wind flow variables at C1 in August 2017, combined from SLID measurements (01-13 Aug) and ULID measurements (14-31 Aug), show (Fig. 2) high day-to-day variability with the strongest wind speeds during overnight period on 5, 16, 20-21 August, which were observed

Accepted for publication in *Journal of Applied Meteorology and Climatology*. DOI 10.1175/JAMC-D-22-0128.1.

to come from the south (Fig 2 a, b). By the end of the month, the mostly north-north-easterly (NNE) winds tended to be weaker. Table 2 shows days grouped by the strength of the nocturnal wind speed in the first 1 km AGL (above ground level), along with the prevailing wind direction for these days.

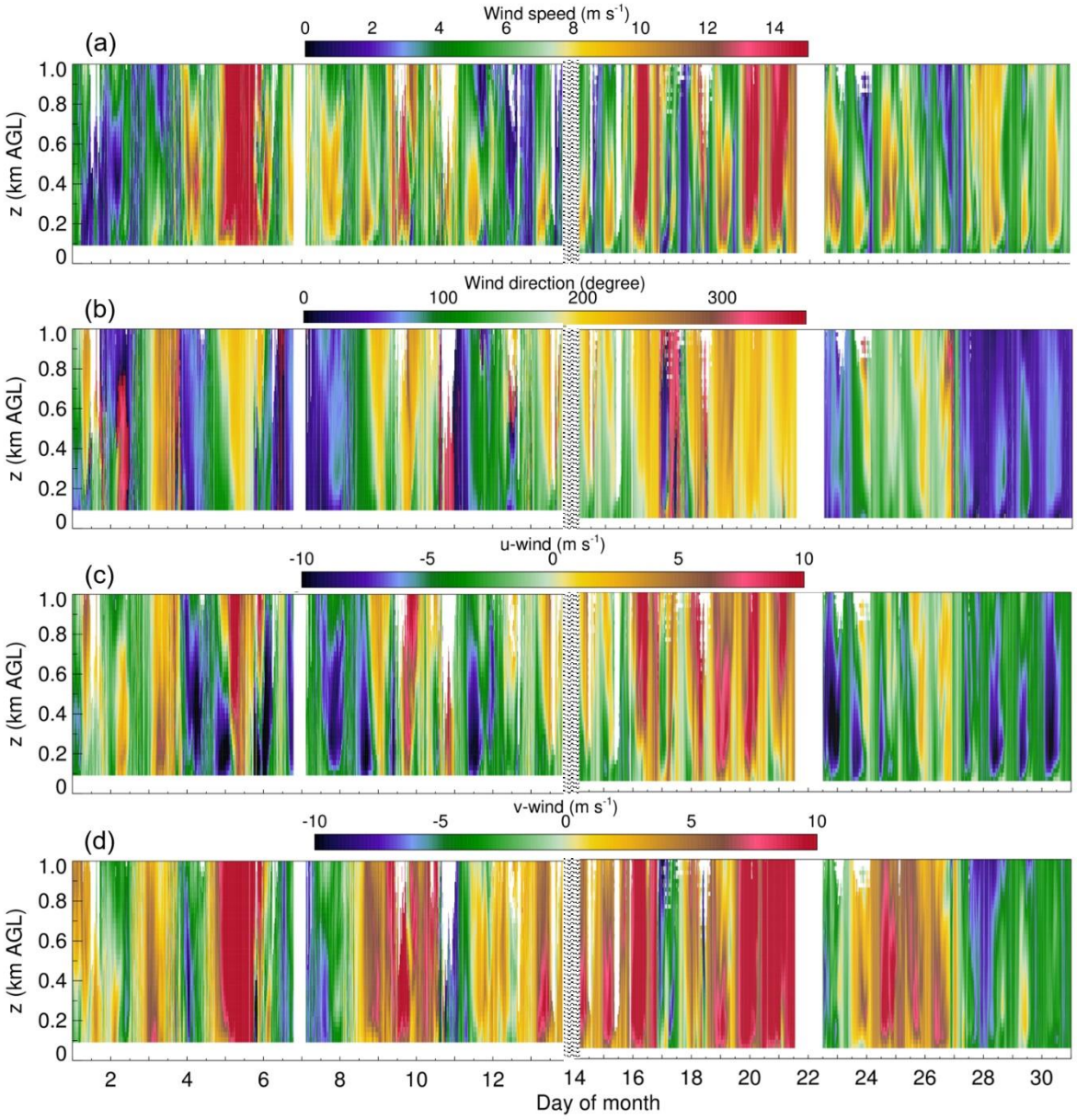

Fig. 2. (a) Wind speed, (b) wind direction, and (c-d) vector wind components for the 1-31 August 2017 from lidar measurement at the central facility (C1). White stripes indicate missing data. Wavy strips around day 14 indicate the transition from SLID (1-13 August) and ULID (14-31 August) measurements. The first available height from the SLID lidar is 90 m. Data from ULID (2 Hz) are averaged over 15-min to fit the temporal resolution of winds from SLID and are plotted from the third height of 53 m due to noisy data at the first two heights.

We can classify the study nights depending on their maximum wind speed, as strong (>12 m s^{-1}), moderate (8-12 m s^{-1}), and weak (<8 m s^{-1}). Figure 3 shows 24-h time-height cross-

Accepted for publication in *Journal of Applied Meteorology and Climatology*. DOI 10.1175/JAMC-D-22-0128.1.

sections of wind speed and direction along with the time-series of those variables at seven heights from 117 to 714 m AGL for one sample day from each category. The differences in wind speed among the levels show the strong shear at night becoming near zero in the local morning after 1600 UTC. The direction time series show that the turning of the wind both with height and with time were mostly small through the 117-714 m layer, which was true for most nights, as further discussed below.

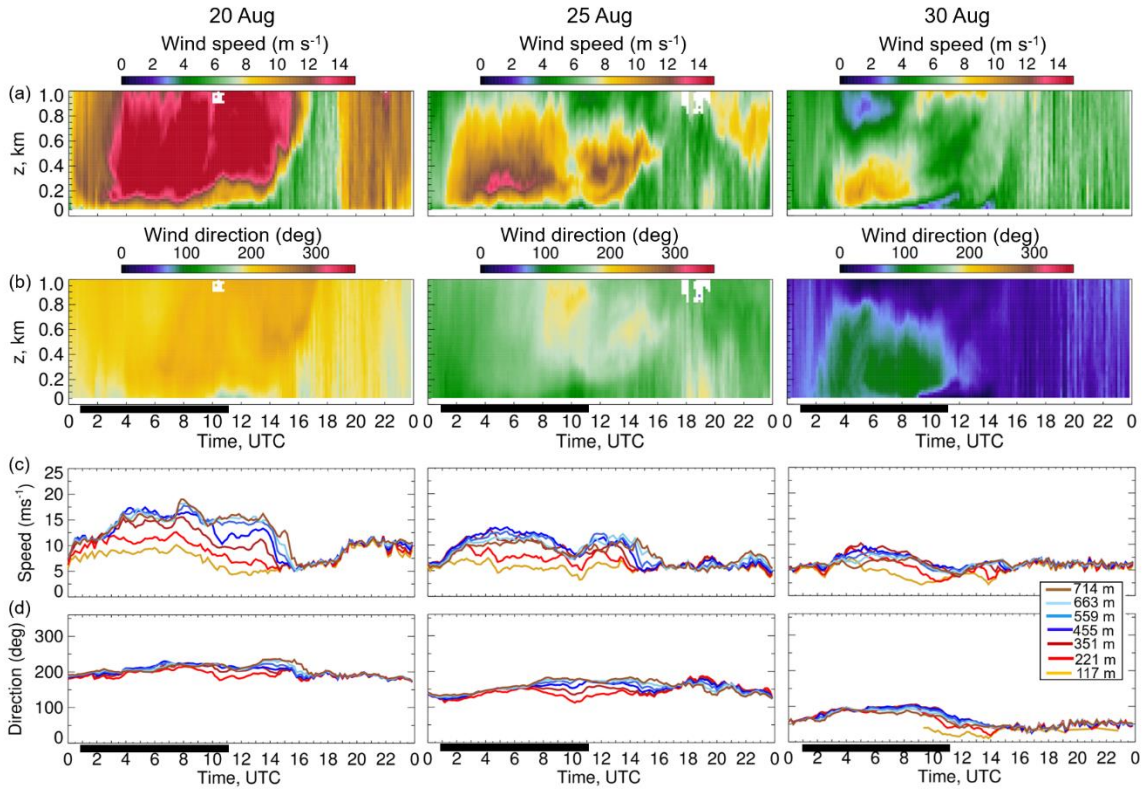

Fig. 3. Diurnal variability of the wind field (a, b) in the first 1 km AGLat site C1 and (c, d) at the seven heights within this layer are shown for 3 days selected from each group: strong, southerly (20 Aug), moderate SE (25 Aug), and weak N-NE (30 Aug) overnight winds. Black and white horizontal bars at the bottom of panels (b, d) indicate night and day hours. Sunrise for the 20, 25, and 30 Aug was at 0653, 0057, and 0701 CDT (UTC-5h); sunset for these days was at 1614, 1608, and 1601 correspondingly. White spots (20 Aug, 25 Aug) above 800 m indicate missing data.

Table 2 lists the nights in August 2017 that fell under each category. Those typical summer nights when the winds were predominantly southerly comprised the strong-wind cases, whereas the postfrontal occurrences where easterly-component flow predominated, which we will refer to as *northeasterly* (*NE*) nights, were the moderate-wind nights. The weak (4-8 m s^{-1}) winds varied over a wide range of directions from northerly through westerly.

Accepted for publication in *Journal of Applied Meteorology and Climatology*. DOI 10.1175/JAMC-D-22-0128.1.

Strong winds 12-25 m s^{-1}		Moderate winds 8-12 m s^{-1}		Weak winds 4-8 m s^{-1}		Excluded days	
Day	**Dir**	**Day**	**Dir**	**Day**	**Dir**	**Day**	**Bad / No data**
5	E-SE-S	***4***	NE	***1***	NE-E-SE	***11***	Rain, bad data
6	S-SE	***7***	E	***2***	SE-S	***17***	Bad data
10	SE-S	***8***	NE-E	***3***	E-SE	***22***	no data at C1
16	SE-S	***9***	E-SE	***12***	N-NE		
19	S	***23***	E	***13***	E-SE		
20	S	***25***	E-SE	***14***	SE-S		
21	S	***26***	E-SE	***15***	SE		
				18	SW-W		
				24	E-SE		
				27	SW-W		
				28	N		
				29	N-NE		
				30	N-NE		
				31	NE		

Table 2. Classification of the LAFE days by the nocturnal wind speed and the prevailing wind direction in the first 1 km AGL (above ground level) from Doppler lidars operated from C1.

To characterize the anomalous nature of wind flows during LAFE, we will compare this period to winds from the 2016-2021 summer months using the long-term SLID data at all sites (Fig. 4). In the next subsection (3.1), we consider large-scale properties of the flow by looking at wind speed and direction averaged over a deep layer. In Subsection 3.2 we look more closely at these properties during August 2017.

3. Summertime nocturnal-wind properties through the SBL.

Unlike typical summers when southerly flow dominates, southerly- and northeasterly-flow days from August 2017 had a roughly equal number of occurrences, allowing flow and LLJ properties to be contrasted between the regimes. The August 2017 LAFE study period was marked by an unusually large number of cold-front passages (including a day-long rain event on 11 August), which disrupted the typically frequent occurrence of southerly LLJs (the definition of LLJs and LLJ parameters is later explained in section 4.1). Large-scale conditions during this month featured many days having a breakdown of the normal Bermuda high-pressure system in the eastern U.S., and an unusually large incidence of hurricane and tropical cyclone systems in the western Gulf of Mexico (see online supplementary material). To

Accepted for publication in *Journal of Applied Meteorology and Climatology*. DOI 10.1175/JAMC-D-22-0128.1.

characterize the anomalous nature of wind flows during LAFE, we will compare this period to winds from the 2016-2021 summer months using both the long-term SLID data at all 5 sites and ULID data at C1 from LAFE (Fig. 2).

3.1. Six summers (2016-2021): 100-700-m layer-mean winds

Figure 4 shows the distributions of 0000-1400 UTC (period of observed LLJs) wind speed and direction averaged for the 117-714-m layer at the five SGP sites. Wind speeds had high frequencies in the range of 4-12 m s^{-1} for all months, which is important for the operations of the nearby wind farms (Fig. 1b) as these winds are in the ascending part of the power curves for most wind turbines (GE Energy, 2009), and the power generated increases proportionally to the cube of the wind speed (Pichugina et al, 2019). Typical summertime months showed a strong, often mono-modal peak in wind *direction* from the south; however, a noticeable secondary peak of north-easterly or easterly winds can be seen during some months, such as July 2018 and July 2019. During the LAFE period (August 2017), the abnormal northeasterly peak was so large that it exceeded the southerly peak, although the southerly peak was broader (Appendix B, Fig. B1). The bi-modal distributions of wind direction in Aug 2017 were also observed at 10-m from 3 EBC flux stations as well as from sonic anemometer measurements at 25 m and 60 m of a tall tower located at C1 (not shown). The patterns appeared similar from site-to-site for each month, but the highest and westernmost site (E37) showed the greatest frequency of strong (>12 m s^{-1}) wind speeds during most months.

Accepted for publication in *Journal of Applied Meteorology and Climatology*. DOI 10.1175/JAMC-D-22-0128.1.

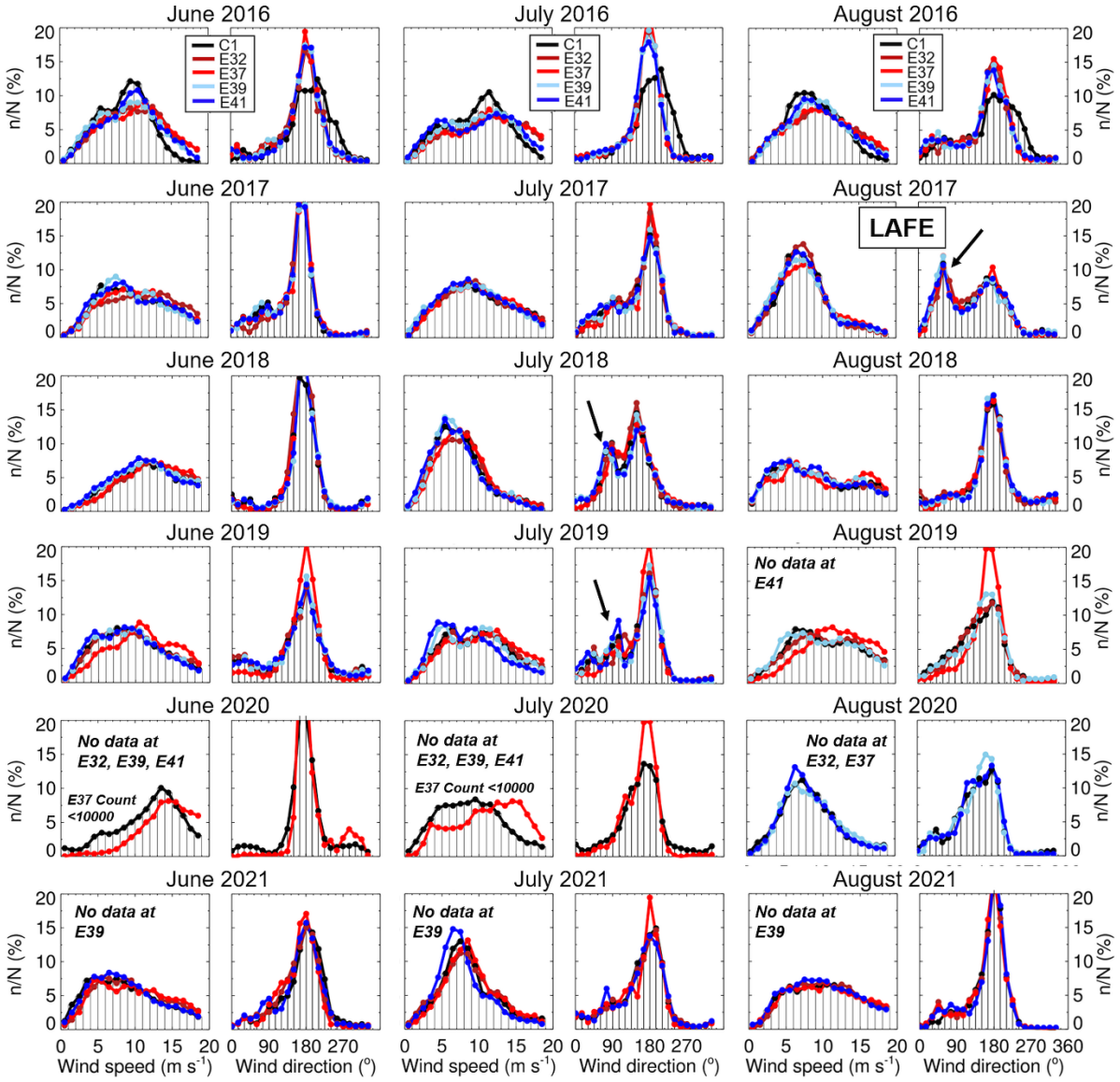

Fig. 4. Distributions of 0000-1400 UTC wind speed and wind direction in the layer of 117-714 m at 5 SGP sites are shown for the summer months of 6 years, from 2016 to 2021. Each site is shown by color according to the legend at the top row. Each plot consists of 15-min profiles at C1 and 10-min profiles at the other four sites. Sites with missing measurements are indicated for each month from Aug 2019 to Aug 2021.

These basic month-to-month variations in mean winds are summarized more quantitatively in Fig. B2 (Appendix B), which shows mean wind speeds and the number of points (integrated over the histograms in Fig. 4) for each month of the six summers. The plots are shown for all wind directions and two sectors (NE and S). Wind speeds from the total sample (Fig. B2a) were mostly 8-12 m s^{-1}. Each year, the strongest winds were southerly (Fig. Bc) at all sites, whereas the north-easterly-component sectors (Fig. Bc) tended to be weaker by 3-4 m s^{-1}. Overall, the inter-annual variability of monthly-mean summer winds in the 100-700-

Accepted for publication in *Journal of Applied Meteorology and Climatology*. DOI 10.1175/JAMC-D-22-0128.1.

m layer was greater than the wind variability among sites (Fig. 4); namely, the variability was ~4 m s^{-1} for the former and 1-3 m s^{-1} for the latter.

The next section provides details of wind flow variability among sites during August 2017.

3.2 LAFE period layer-mean wind-flow conditions.

The dichotomy in wind direction between the normal and postfrontal regimes for the LAFE period is clear from the August 2017 wind roses for the first 700 m AGL - the layer most covered by lidar measurements at all sites (Fig. 5a). Higher frequencies of winds from NE and S-SSE sectors than other directions at each site is highlighted by the dark yellow lines on C1.

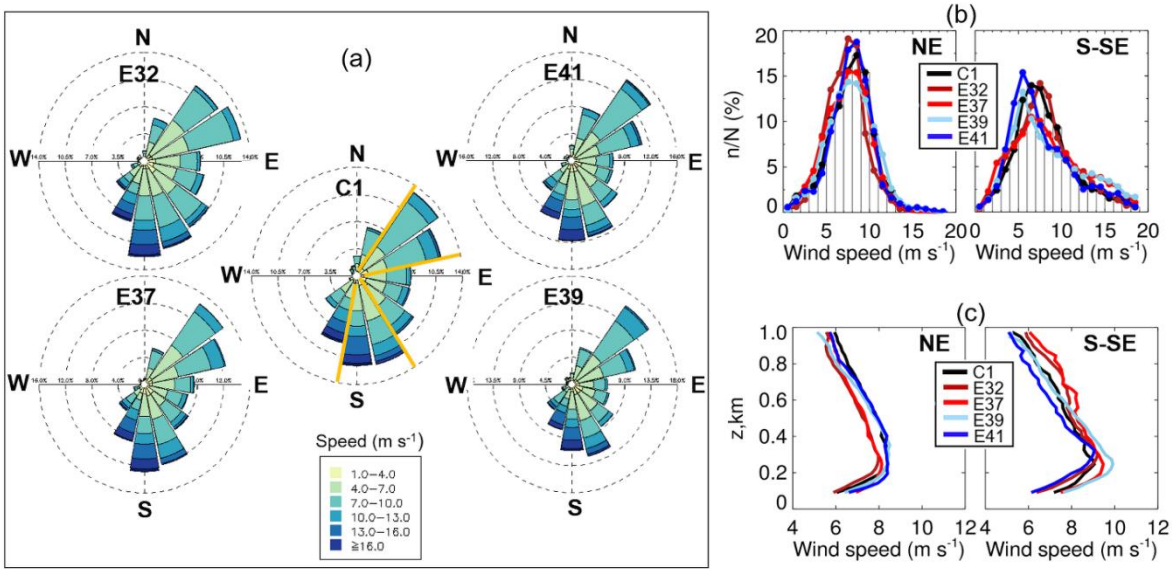

Fig. 5. Overnight (0000-1400 UTC) winds for August 2017 at the 5 SGP sites. (a) Wind roses in the first 700 m AGL. (b) Distributions of wind speed in two sectors of wind direction, which are highlighted by dark yellow lines at C1 (Fig. 6a), NE (33.7º-78.7º), and S-SE (146.2º-191.3º). (c) Mean profiles in the same sectors as (b).

Distributions of wind speed (Fig. 5b) for the S-SSE sector show a broader range of speeds and a larger fraction of winds greater than 11 m s^{-1}, as compared to the NE wind regime. August-mean profiles (Fig. 5c) for these sectors show LLJ shapes having maxima around 200 m (NE) and 225-300 m (S-SSE) AGL. The NE winds at the 200-m jet height were 7.8 m s^{-1} at the western E32 and E37 sites, compared to 8.2 m s^{-1} at the other sites, and speeds continued to be about 0.5 m s^{-1} weaker above. The difference in S-SSE winds among sites varied with height AGL, the western sites being comparable to the others below 500 m, but 1 m s^{-1} stronger above

Accepted for publication in *Journal of Applied Meteorology and Climatology*. DOI 10.1175/JAMC-D-22-0128.1.

500 m. At LLJ heights the winds at the southern (E37, E39) sites (~10 m s^{-1}) were ~1 m s^{-1} stronger than those at the northern (E32, E41) sites (~9 m s^{-1}).

Overall no significant differences were found between the wind relationships at different sites when comparing 0000-1400 UTC and the 24-h (0000-2400 UTC) periods (Tab. 3) at eastern and western sites as well as the southern and northern sites. A high correlation was found for winds in the larger layer 90 m-714 m AGL for both 0000-14000 (R^2= 0.84-0.85) and 24-h (R^2= 0.83-0.84) periods.

Compared sites	**90 m - 714 m layer**													
	0000-1400 UTC							0000-2400 UTC						
	R^2	**Count**	**A**	**B**	**Site**	**Mean**	**STD**	**R^2**	**Count**	**A**	**B**	**Site**	**Mean**	**STD**
	East sites vs. West sites													
E41 vs E32	0.84	17749	1.11	0.84	E32	7.61	3.80	0.83	30820	1.02	0.82	E32	6.85	3.62
					E41	7.48	3.79					E41	6.64	3.60
E39 vs E37	0.84	19189	1.19	0.81	E37	8.00	4.10	0.84	32317	1.28	0.79	E37	7.14	3.96
					E39	7.69	3.96					E39	6.89	3.72
	North sites vs. South sites													
E37 vs E32	0.85	17285	1.05	0.91	E32	7.62	3.81	0.83	29716	0.98	0.90	E32	6.86	3.64
					E37	8.00	4.08					E37	7.14	3.93
E39 vs E41	0.84	20162	1.08	0.88	E41	7.51	3.81	0.83	34377	1.21	0.85	E41	6.64	3.65
					E39	7.67	3.97					E39	6.86	3.72

Table 3. Spatial variability of wind speed in the layer 90 m-714 m between east/west and north/south SGP site for 0000-1400 UTC hours and over the diurnal cycle. The num (Count) of profiles in Aug 2017 was used for the calculation of the correlation coefficient (R^2) between wind speed at two sites and the coefficients of the linear fit (y=A+Bx). Mean and standard deviation (STD) are computed over two periods (0000-1400 UTC) and (0000-2400 UTC) and are shown for winds in two layers: 90-714 m and 90-117 m.

In wind energy operations winds at the hub-heights of wind turbines have often been used to estimate the power production of a wind farm. In Aug 2017 wind roses of the 117-m wind speed (Appendix C) show similar patterns for the 0000-1400 UTC and the 24-h (0000-2400 UTC) periods at all sites, with stronger S-SSE winds, and a significant frequency of NE winds. The high frequency (>70 %) of 4-12 m s^{-1} winds was observed within the layer at 90 and 117 m AGL – the layer of hub-heights of modern wind turbines (Appendix D, Table D). The very weak wind (0-4 m s^{-1}) group is also included in this table to indicate how often turbines may not operate due to winds below cut-in values (GE Energy, 2009). The range of these cases (20-28%) means that turbines would not have been harvesting winds for about 104-

Accepted for publication in *Journal of Applied Meteorology and Climatology*. DOI 10.1175/JAMC-D-22-0128.1.

202 hours in August 2017. Such slack conditions are good for maintenance and repair operations if they can be forecasted.

4. Low-Level Jet properties during LAFE (August 2017)

4.1. LLJ statistics from lidar measurements

Wind-profile measurements from scanning Doppler lidars at the five SGP sites obtained with high temporal (10-15 min) and vertical (~21 m) resolutions are used to statistically characterize LLJ properties (Fig. 6a) including jet-speed maxima (U_{LLJ}), the height of these maxima (Z_{LLJ}), wind direction at this height (D_{LLJ}), and overnight evolution of these parameters for different wind-speed regimes (as illustrated in Fig. 3).

The occurrence of LLJs in each wind speed profile was estimated by an automated procedure that detects wind speed maxima (U_{LLJ}) with a decrease of at least 2 m s^{-1} at vertical levels both above and below the level of the peak value (Z_{LLJ}), the criteria proposed in Andreas et al. (2000).

Similar to the other parts of the Great Plains (Banta et al 2002, 2003, Kelley et al, 2004; Gebauer et al. 2018; Smith et al. 2018, 2019; Carroll et al. 2019), summer LLJs at SGP sites generally formed over a 3-h period after sunset (2030-2130 CDT, 0230-0330 UTC). In August 2017 LLJs at SGP sites were frequently identified during 0000-1400 UTC from various shapes (Fig. 6b) of wind profiles (Pichugina et al. 2010). The "classic" LLJ (Fig. 6d, 0900 UTC), single-maximum shapes occurred often during stable BL conditions at 0300-1000 UTC for many nights, although sometimes such profiles were observed up to 1200 UTC. Multiple maxima in the wind-speed profile were occasionally observed after dawn, during morning-transition (1000-1400 UTC) hours (Fig. 6d, 1400 UTC), under neutral, near-neutral, or unstable conditions at the surface. This structure was generally related to the growing early-morning shallow convective boundary layer eroding the LLJ layer from below.

In addition to the nocturnal evolution, LLJ parameters were analyzed for three periods: evening transition (0000-0300 UTC), nighttime (0300-1000 UTC), and morning transition (1000-1400 UTC). Stability was estimated by the Monin-Obukhov Length (L_{MO}) obtained from sonic-anemometer measurements at the 25-m and 60-m levels of a tower installed at C1. An example of diurnal wind speeds in the first km AGL on 19 August illustrates LLJ development through the night (Fig. 6c).

Accepted for publication in *Journal of Applied Meteorology and Climatology*. DOI 10.1175/JAMC-D-22-0128.1.

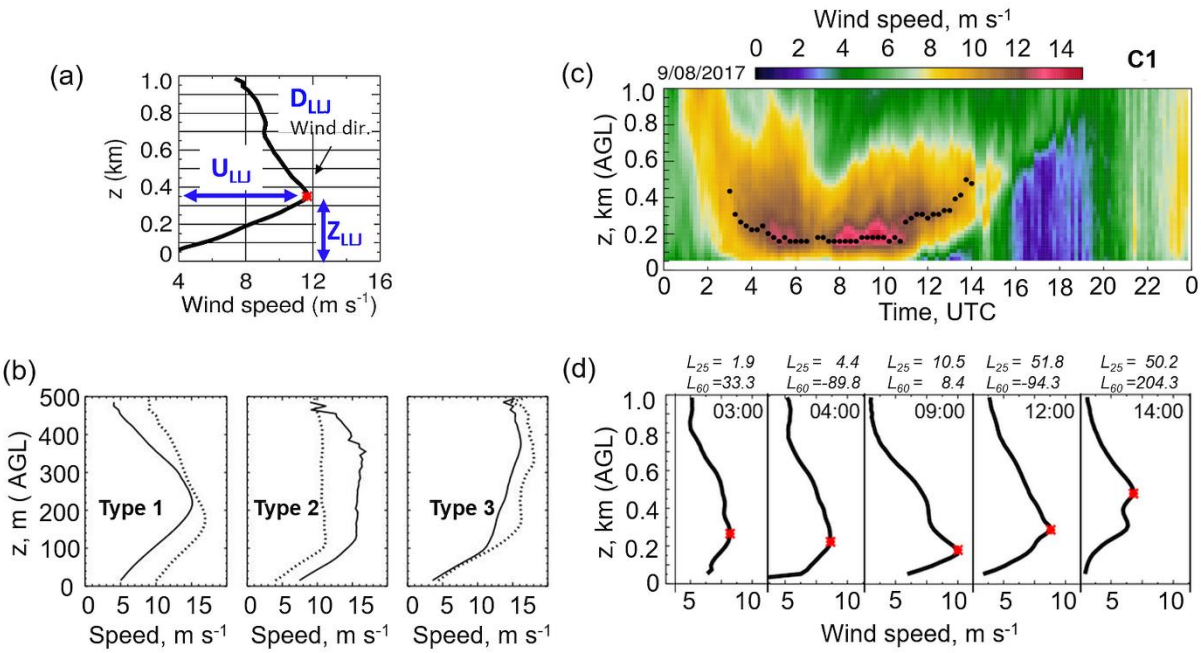

Fig. 6. (a) Definition of LLJ parameters. The red point indicates the LLJ strength (U_{LLJ}) and the LLJ height (Z_{LLJ}) automatically detected in each 15-min wind profile. The LLJ direction (D_{LLJ}) is the value in wind direction profile found for this time and at this height. (b) Categories of wind profiles frequently observed from lidar measurements during the previous experiments in the Great Plains (from Pichugina et al, 2010; AMS). (c) Time-height plot of wind speed on 19 Aug 2017 at C1. Black symbols indicate the LLJ evolution. (d) Sample wind speed profiles most observed during dusk (0000-0300 UTC), nighttime (0300-1000 UTC), and morning-transition (1200-1400 UTC) periods on 19 Aug.

Nighttime winds on this day were southerly and moderate (8-13 m s^{-1}) in the first 700 m AGL, the strongest LLJ speeds occurring at ~200 m at 0800-1100 UTC. Sample profiles from each period (Fig. 6d) illustrate both how the algorithm estimates LLJ properties and how the wind profiles develop from a late-afternoon (0000-0300) mixed-layer through a nighttime (0300-1000) LLJ and to the (1000-1400) morning transition profiles (where in these unstable-BL profiles, the upper maximum is indicated).

Distributions of LLJ properties in August 2017 (Fig. 7a) show the highest frequency of strong (>12 m s^{-1}) jets during nighttime hours (0300-1000 UTC), and a significant portion of the jet maxima for all 3 periods was located at 200-300 m.

Accepted for publication in *Journal of Applied Meteorology and Climatology*. DOI 10.1175/JAMC-D-22-0128.1.

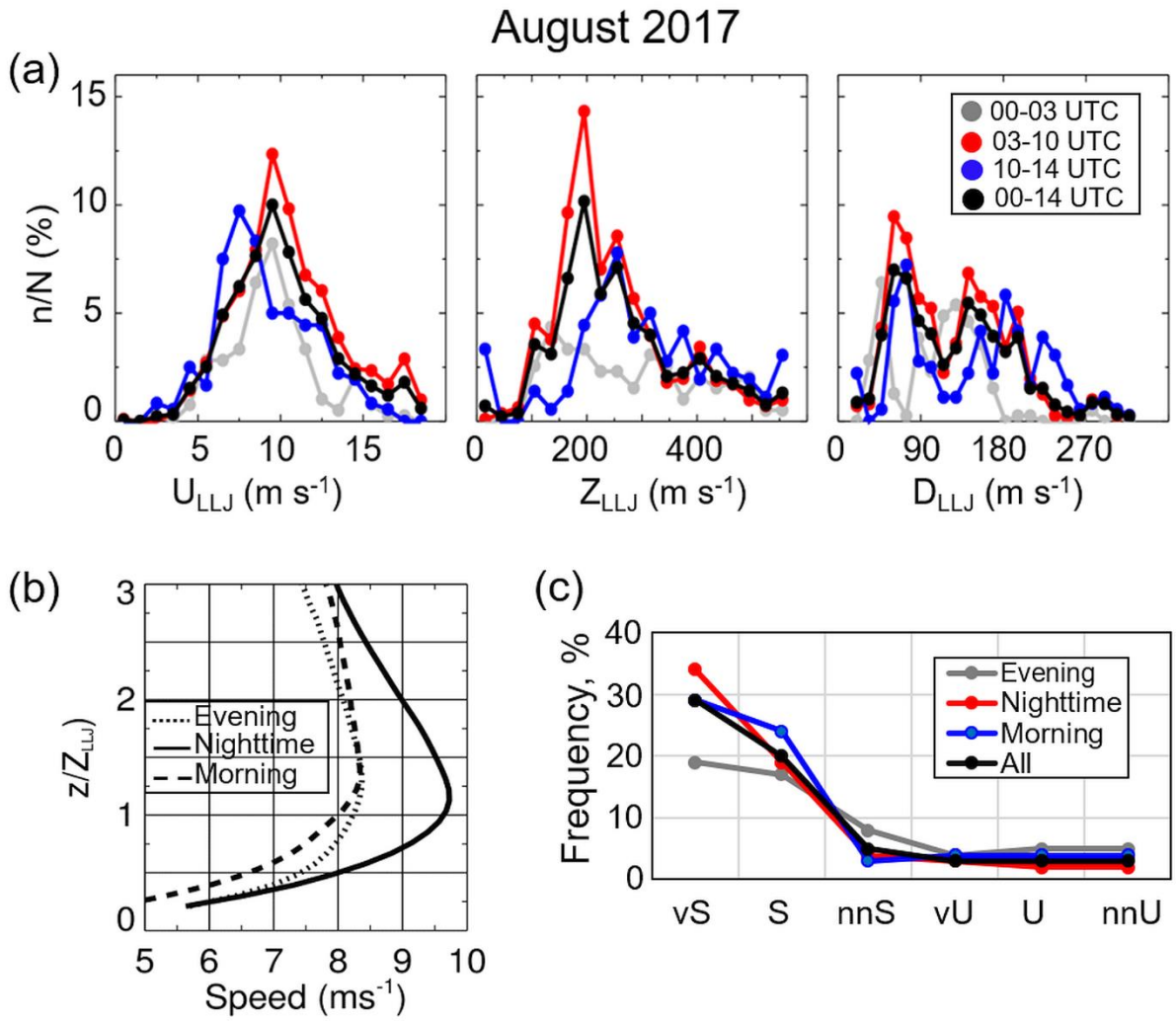

Fig. 7. (a) Distribution of LLJ parameters in Aug 2017 from measurements at C1 for three periods (000-0300, 0300-1000, and 1000-1400), and over 0000-1400 UTC. (b) Monthly-mean profiles of wind speed at C1 normalized by the height of LLJ (Z_{LLJ}) are shown for each of 3 periods. (c) The frequency (%) of the stability classes based on the L_{MO} (Tab. E, Appendix E) from sonic anemometer data at 25 and 60 m of an 80-m tower is shown for periods as in Fig. 7a.

Monthly-mean profiles normalized by Z_{LLJ} (Fig. 7b) illustrate LLJ-profile shapes having strongest U_{LLJ} during the nighttime hours.

Distributions of D_{LLJ} show two prevalent (NE and S-SSE) directions for each period. Mean LLJ statistics from Fig. 7a (Table 4) show a significant number of LLJ profiles with a mean frequency of 38, 74, and 59% for the evening transition, nighttime, and morning transition hours. The most frequent stability conditions for the evening, nighttime, and morning hours in August 2017 were (Fig. 7). very stable (19, 34, and 29 %) and stable (17, 19, and 24 %), respectively.

Accepted for publication in *Journal of Applied Meteorology and Climatology*. DOI 10.1175/JAMC-D-22-0128.1.

Period (UTC)	Mean U_{LLJ}	Mean Z_{LLJ}	Mean D_{LLJ}	LLJ frequency (%)
0000-0300	9.4±2.7	290±145.3	120±54.9	38
0300-1000	10.6±3.5	248±124.8	139±68.0	74
1000-1400	9.9±4.5	323+166.5	169±86.8	59
0000-1400	10.4±3.7	266+140.1	141±71.2	64

Table 4. Mean LLJ statistics for August 2017 at C1 (Fig. 7a) are shown for different periods: late-afternoon (0000-0300), nighttime (0300-1000) LLJ, and the morning transition (1000-1400, where in these unstable-BL profiles, the upper maximum is indicated), and the overnight (0000-1400 UTC) period.

4.2 Spatial variability of LLJ parameters in August 2017

Wind-flow patterns among the sites for 23 August LAFE IOP 11 are shown in Fig. 8, which shows that many details of LLJ evolution varied among sites. Differences are evident in the timing of the LLJ, the maximum height of the jet nose, and the strength and depth of LLJs (Fig. 8f). This day of primarily easterly winds is characterized by a disturbance at ~ sunset (e.g., 0100-0400 UTC at E37 and E32, then 0500-0700 UTC at E39) and shown here, as it was an important day for other LAFE studies.

Figure 9a shows LLJ wind roses for August 2017 at the five SGP sites. The predominant LLJ directions were from the south or northeast, and the strongest jets (darkest blue shading) were from the south (*cf.* Gebauer et al. 2017; Carroll et al. 2019), consistent with the layer-averaged mean winds (Fig. 5). Small site-to-site differences can be seen in the prevailing direction of the southerly flow occurrences: the westernmost sites show mostly southwesterly LLJ-nose directions, whereas the mode for E41 was southerly and for C1 and E39, SSE. Distributions of U_{LLJ} (Fig. 9b) are similar in shape and monthly mean values (9.8-10.2 m s^{-1}). The distribution of LLJ directions (Fig. 9b) at the jet nose shows a significant NE component in addition to the more normal southerly (SSE through SSW) jets, again consistent with the ~100-700-m layer mean wind-speed (Fig. 5). Site-to-site variability is evident in the shapes

Accepted for publication in *Journal of Applied Meteorology and Climatology*. DOI 10.1175/JAMC-D-22-0128.1.

and mean values of the bi-modal distributions of Z_{LLJ} and the wind direction (D_{LLJ}) at the height of LLJs.

Inter-annual comparisons of LLJ parameters (Fig. 10) show that in general, jet speeds were smallest in 2017, but for each year agreed within ~ 2 m s^{-1}among the sites, with jet height varying over ~100 m. Similar to Fig. 9b, a closer relative agreement is seen in the strength (U_{LLJ}) and direction (D_{LLJ}) of LLJs between sites for all years compared to the height (Z_{LLJ}) of LLJs, where, e.g., larger (~200 m) differences can be seen between E37 and E41 in Aug 2016 (after 1000 UTC). Mean wind directions at all sites and years showed modest veering from SEly at the evening transition towards the S and SW by 1400 UTC. The modest LLJ veering in the evening hours was also observed from CASES-99 and LLLJP-03 (e.g., Pichugina and Banta 2010). Overall, in the LAFE month of August 2017, LLJs at all five sites were weaker, lower, and more easterly compared to other years.

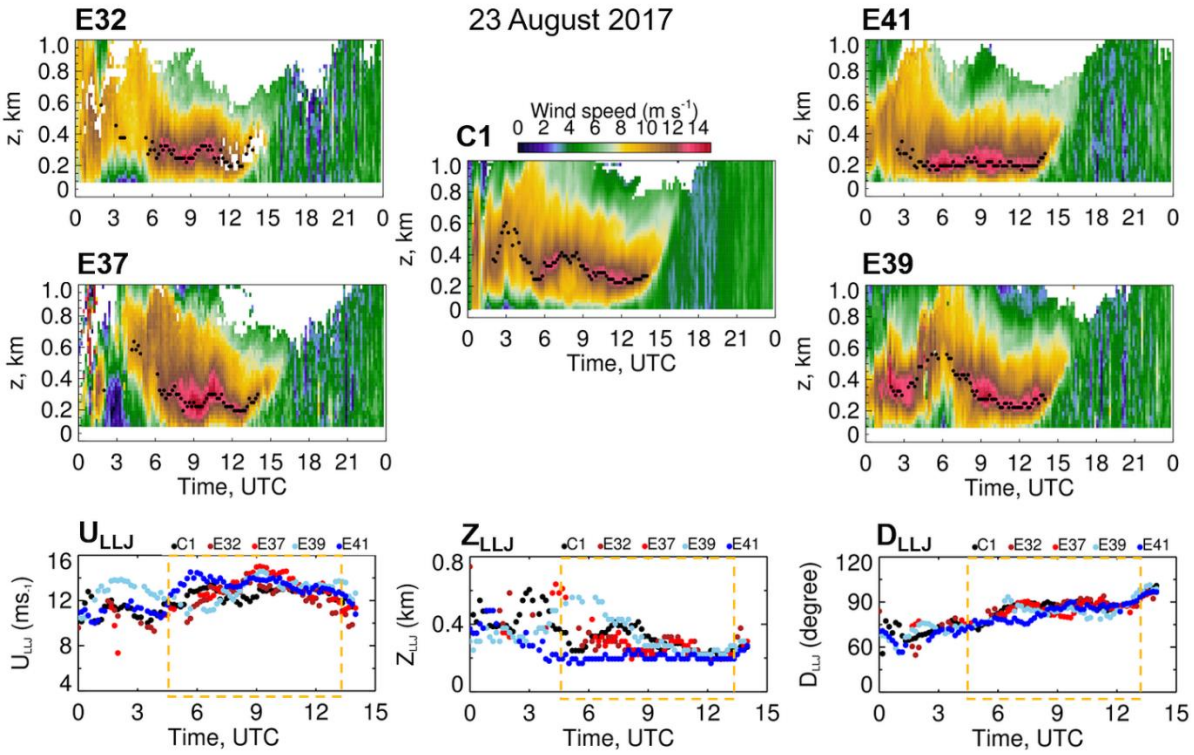

Fig. 8. (a-e) Time-height cross-sections of wind speed on 23 August from lidar measurements at 5 SGP sites. Panels for each site are plotted following the location of sites (Fig. 1) to better illustrate the connection of wind flow and LLJ difference to the site's position (S-N and W-E) and surface types. The height of the LLJ is indicated by black symbols for 0000-1400 UTC. (f) Time-series of the LLJ properties U_{LLJ}, Z_{LLJ}, D_{LLJ} at 5 sites are shown by colors as indicated at the top of each panel. The dark golden box outlines the period of very stable (vS) and stable (S) boundary layer conditions observed on 23 Aug.

Accepted for publication in *Journal of Applied Meteorology and Climatology*. DOI 10.1175/JAMC-D-22-0128.1.

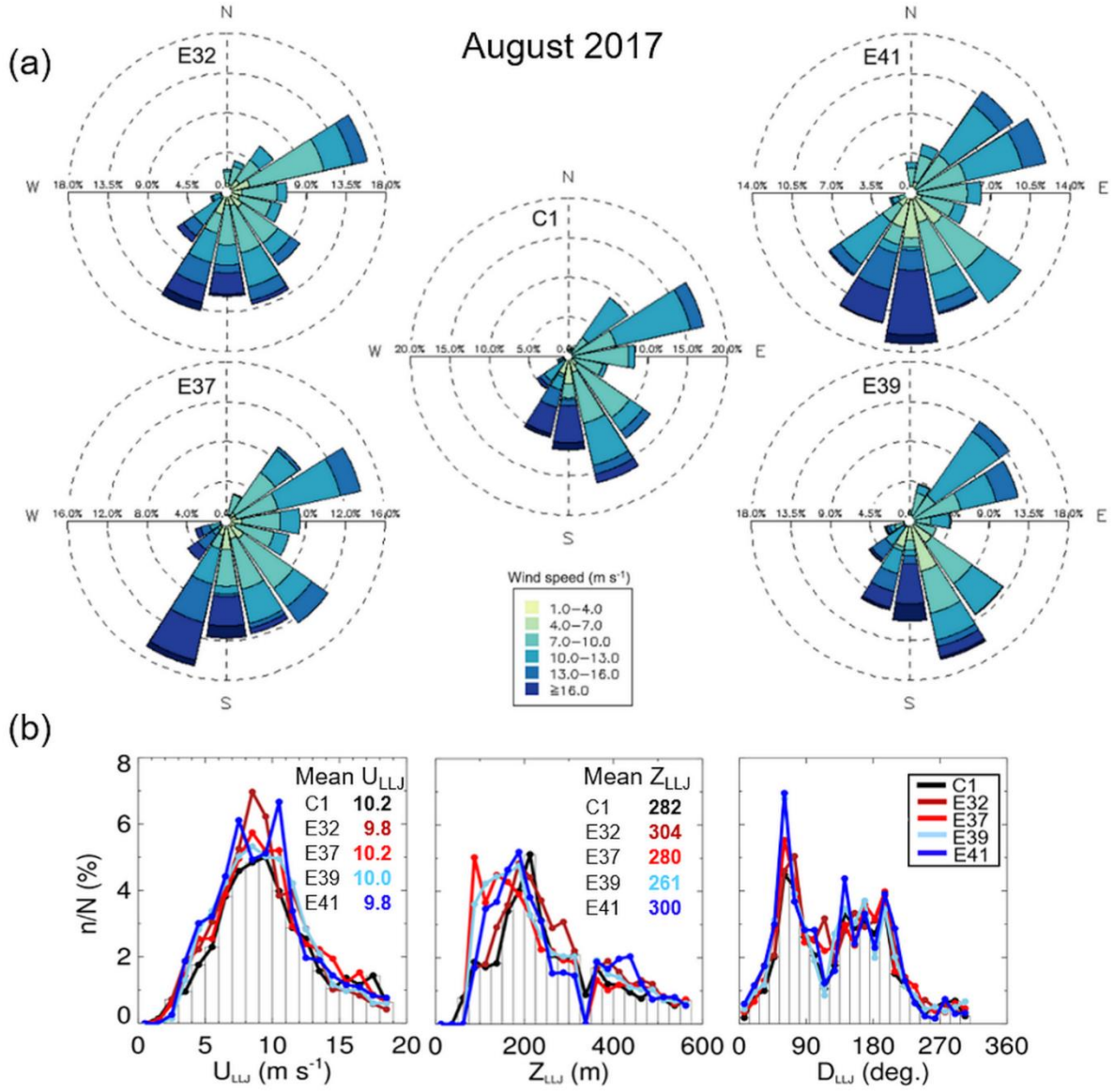

Fig. 9. (a) Wind roses of U_{LLJ} in August 2017 at 5 SGP sites for 0000-1400 UTC. (b) Distributions of LLJ parameters over 0300-1400 UTC in August 2017 at 5 sites. The mean values of U_{LLJ} and Z_{LLJ} at each site are given by the corresponding color.

Accepted for publication in *Journal of Applied Meteorology and Climatology*. DOI 10.1175/JAMC-D-22-0128.1.

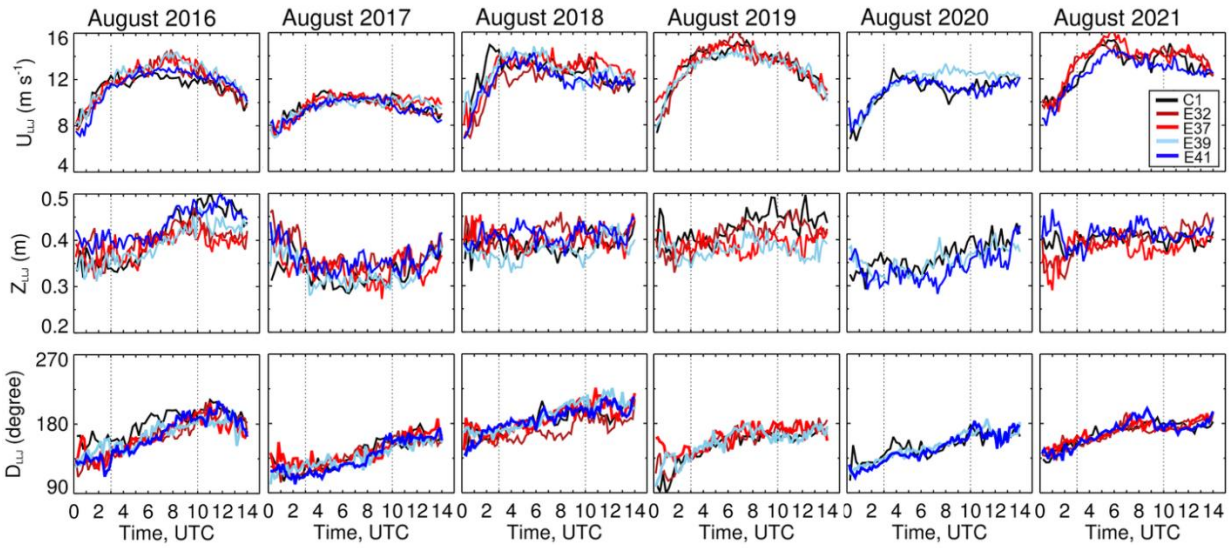

Fig. 10. August-mean LLJ properties at 5 sites are shown for 2016-2021. LLJ parameters (from top to bottom) U_{LLJ}, Z_{LLJ}, and D_{LLJ} at each site are shown by color lines according to the scale at the right top panel. Missing data on 2019 and 2020 at some sites are due to instrument maintenance.

4.3 Relationship between turbulence and LLJs

All mechanisms for generating nocturnal LLJs require an abrupt reduction of vertical turbulent momentum-flux divergence at sunset. Although the turbulent fluxes are reduced by at least a factor of 10, they do not go to zero. Likely, the magnitude of the fluxes—and as a consequence, the magnitude of this reduction—as well as the structure of the post-sunset flux profile through the SBL play key roles in the nighttime balance of forces. NWP models need to get this right, and it is, therefore, important to investigate the turbulence structure of the nighttime SBL, in an attempt to understand the role of the turbulence profile in the dynamics of the LLJ. Turbulence parameterizations are acknowledged weaknesses of NWP models, so for studies of these processes, accurate measurements of mean and turbulent momentum profiles are required to advance understanding of LLJ-SBL dynamics and to assess the credibility of model results.

The LLJ generates a strong shear zone and thus strong shear-generated turbulence between the LLJ nose and the surface. It is essential to distinguish between the height of the LLJ speed maximum, or jet nose Z_{LLJ}, and the height of the turbulent SBL Z_h. Mahrt et al. (1979) noted that Z_{LLJ} represents an "upper bound to the vertical extent of turbulent transport," because of the peak in stability (Ri) at this level, and refer to it as the top of the "momentum boundary layer." Referring to Z_{LLJ} as an "upper bound" recognizes that significant turbulence

Accepted for publication in *Journal of Applied Meteorology and Climatology*. DOI 10.1175/JAMC-D-22-0128.1.

does not always extend up to this level. Other studies have attempted to equate the jet nose with the top of the SBL Z_h. For weakly stable SBL conditions Banta et al. (2006) showed a high correlation between Z_{LLJ} and minima in the turbulent velocity-variance profile. But Banta et al. (2002) noted that wind-speed profiles can have many shapes, some having multiple maxima. The height of the first wind speed maximum above the surface in Banta et al. (2002, 2003), which was not always the absolute maximum speed (i.e., Z_{LLJ}), was considered a good representation of the depth of the surface-based shear layer, and by inference of Z_h itself (also Balsley et al. 2006).

Pichugina and Banta (2010) showed that the relationship between Z_{LLJ} and Z_h was even more nuanced. Because of the lack of directional shear with height and the relative flatness of the terrain, they were able to use lidar along-wind scans in elevation (vertical-slice or "RHI" scans) to profile the mean wind speed and streamwise variance, which was found to be approximately equal to TKE for stable conditions (Banta et al. 2006; Pichugina et al. 2008). The advantages of this scanning approach were that each scan took ~30 s (or less) to complete. Each 10-min averaging period thus contained a large sample of points from at least 20 scans, so that even using 5- or 10-m vertical binning, the analysis produced smooth profiles of the wind speed and variance. They used the minimum in the variance profile to define Z_h and related this to features in the mean speed, shear, and curvature profiles. They found three shapes (Fig. 6b) to the wind speed profile, the one in which the wind profile (Type 1) has a distinct nose that corresponds to the top of the SBL Z_h from the variance profile, and a second (Type 2) which has a distinct surface-based layer of strong shear and turbulence but does not have a distinct nose because the profile above this layer has constant speed with height. The third profile shape (Type 3) showed a layered structure to the shear and turbulence, where the strongest values are within a ground-based layer that lies beneath the second layer of weaker (but still positive) shear and weaker turbulence aloft. For these profiles, the maximum jet speed is at the top of the upper layer at Z_{LLJ}, but the SBL Z_h reaches only the top of the lower, strong-shear layer, so in this case, the two do not coincide. The scaling of SBL properties by LLJ speed and height previously proposed (Banta et al. 2003) should be interpreted as the mean speed and height at the top of the turbulent boundary layer Z_h (which would be Z_{LLJ} when the two coincide), as also found for stable conditions in the Netherlands by Vogelezang and Holtslag (1996).

Accepted for publication in *Journal of Applied Meteorology and Climatology*. DOI 10.1175/JAMC-D-22-0128.1.

Many Great-Plains studies have found Z_{LLJ} maxima at 400-500 m or more (e.g., Whiteman et al. 1997; Bonin et al. 2020). These deep jets are certainly well above Z_h, the height to which significant surface-generated turbulence is likely to extend in stable conditions. In measured summertime Great-Plains LLJ profiles of sufficient data quality, the layered Type-3 profile, where the jet nose is higher than the top of the SBL (for example, Bonin et al. 2020), is seen more often than in CASES-99 and LLLJP-03. Figure 11a shows an example of an LLJ profile from 23 August 2017, where the depth of the stronger, surface-based turbulence does not extend up to Z_{LLJ}, but its top can be associated with a kink in the mean vertical shear of the profile, as in the Type-3 profiles. The weaker, shallower LLJs observed during the CASES-99 experiment may reflect the lack of strong surface heating in October at higher elevations of the western Great Plains, such that the east-west temperature differential was too weak to routinely activate an effective thermal-wind mechanism (Parish and Oolman 2010). Conceptually, we may consider the lower, strong-shear layer as a layer where surface-based, mechanically-generated turbulence dominates, but the intensities are much weaker than daytime turbulence, enabling the Blackadar-jet maximum to form at Z_h. The upper layer is where surface-based shear (and turbulence) weakens to the extent that other larger-scale drivers (slope effects, thermal wind—which do not support such large shears), take over (Banta et al. 2002), such that the wind speeds continue to increase with height, but not so strongly as below Z_h.

During LAFE, some of the 15-min profiles under stable conditions show Type I structure when Z_{LLJ} coincides with the height of the minimum turbulence as illustrated by sample profiles (Fig. 11b), but most of the profiles, especially for the deep LLJs, exhibited Type 3 structure.

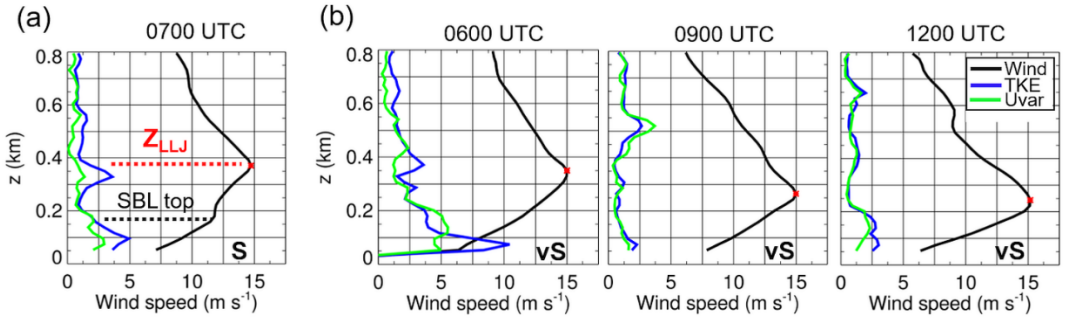

Fig. 11. (a) Sample profiles of (blue) TKE, (green) the horizontal velocity variance, and black wind speed profiles for 0700 UTC on 23 August at C1. The TKE and Uvar data were available from "6-beam" ULID measurements during LAFE. The first minimum of the turbulence indicates the SBL (stable boundary layer) top. The second minimum corresponds to the strongest LLJ height (Z_{LLJ}) indicated by the red symbol. (b) Profiles for 0600, 0900, and 1200 for this night illustrate the most observed cases during the very stable (vS)

Accepted for publication in *Journal of Applied Meteorology and Climatology*. DOI 10.1175/JAMC-D-22-0128.1.

boundary conditions when the minimum of shear-generated turbulence coincides with the Z_{LLJ}, except 0700 UTC on 23 Aug which is similar to (a) stable (S) BL.

4.4 Turning of the wind: Temporal and spatial hodographs.

Temporal hodographs. After the post-sunset drop in the intensity of vertical mixing in the ABL, the horizontal winds above the heights where the LLJ nose forms follow an inertial oscillation (IO) in time about the geostrophic wind according to the theory proposed by Blackadar (1957). The amplitude of the IO decreases with a height from its peak value at the jet nose, and its period corresponds to a half pendulum day $T=2\pi/2\omega\sin\phi$ (~20 h in Oklahoma), where ω is the Earth's rotational frequency and ϕ the latitude. The IO wind oscillation rotates anti-cyclonically (clockwise, Northern Hemisphere) from its late-afternoon direction, which is at an angle down the pressure gradient, to a direction aligned with the geostrophic wind (normal to the pressure gradient) after ¼ period, when it reaches maximum speed. The wind then continues to rotate but at decreasing speeds, as it is now blowing toward higher pressure, until after the morning transition the next day when the daytime balance of forces is restored and the winds become well mixed. Idealized LES model runs have reproduced this behavior (Fedorovich et al. 2017).

On most LAFE nights the turning of the wind in time appeared small at all vertical levels (Fig. 4d), in agreement with previous studies. The I-O theory is concerned with departures from geostrophic, which is difficult to determine with accuracy, so Fig. 12 shows the behavior of the wind direction as a departure from its 0000 UTC value (*cf*. Klein et al. 2015; Bonin et al. 2020) at several vertical levels on an expanded direction axis. Shown are time series of wind directions for the five sites on three southerly-flow nights and two northeasterly-flow nights. For each night the values at the five sites tracked each other rather closely (mostly within 10°), especially on 21 August and the NE flow nights, although instances of flow disruptions at individual locations can be seen, for example, at site E32 from 05-07 UTC and after 10 UTC on 21 August when significant wind shifts (50^O and 100^O respectively) occurred at the lower levels. The Aug. 21 ramp events from lidar measurements and LES are analyzed in a separate study. Similarly, such flow disruptions can be seen at times during the night at site E41 on 20 August at the lower levels.

The NE-flow nights tended to show a steady turning through the night, which was smallest at the lowest 116-m level and which for most of the sites amounted to less than 20° over the entire 12-h (0000-1200) period. For the southerly flow nights, any turning tended to

Accepted for publication in *Journal of Applied Meteorology and Climatology*. DOI 10.1175/JAMC-D-22-0128.1.

occur in the first 6 h, after which the direction remained constant or in some cases reversed. As was the case for the NE-flow nights, the nightly rotation was mostly less than 20°, but again, happening in the first 6 h of 19-20 August. Vanderwende et al. (2015) also found small-magnitude (3° h^{-1}) rotations through the night farther north in Iowa. For these cases, the normal expected strong IO-theory rotation thus clearly did not continue through the night. It is worth noting that all five sites behaved similarly so that each site was representative of regional LLJ evolution.

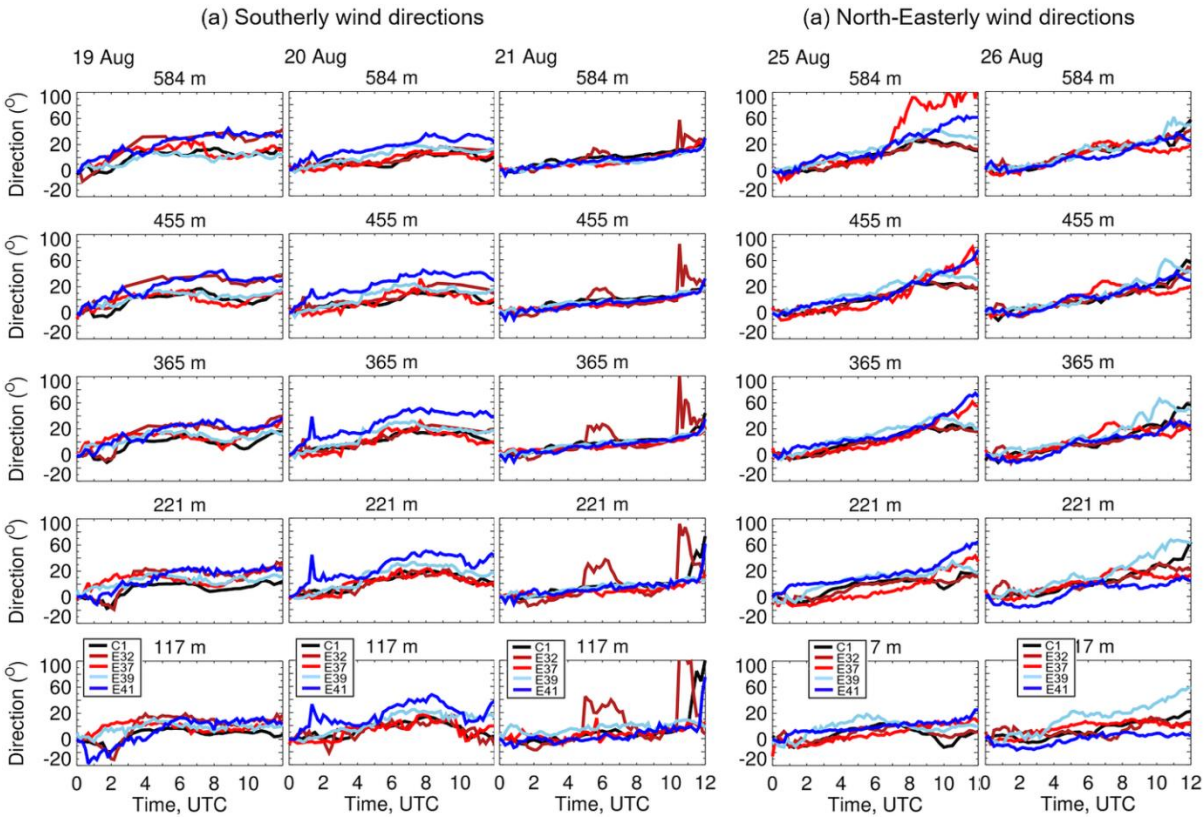

Fig. 12. Directional deviation from 0000 UTC direction for (a) southerly and (b) north-easterly winds at 5 heights (117, 221, 365, 455, and 584 m) through the boundary layer with the most frequent LLJs. Winds at each SGP site are indicated by colors according to legends at the bottom panels.

Temporal hodographs at constant height (Fig. 13) show that at 117 m, which was generally within the turbulent SBL, the evolution of the wind tended to be largely disorganized. At 455 m AGL, above the jet nose, clockwise rotation was found on most nights. On 22 August, the hodograph showed an IO-like rotation, with peak speeds occurring at ~05-06 UTC. Although other southerly nights did have indications of a clockwise rotation, it was not always so obviously IO-like; for example, 22 August had a small rotation in direction but mostly accelerated to >15 m s^{-1} through the night. NE-flow nights also had a mostly disorganized flow

Accepted for publication in *Journal of Applied Meteorology and Climatology*. DOI 10.1175/JAMC-D-22-0128.1.

evolution at 117 m, but at 455 m, some nights, such as 25 August, did have IO-like rotation, although the peak speeds were often later than 06 UTC. On many NE-flow nights, the resemblance to the IO was less clear, such as on 24 August shown here. Thus, nights could be found having temporal hodographs that conformed to the IO pattern, but not consistently: many nights having well-formed LLJs did not clearly exhibit this behavior.

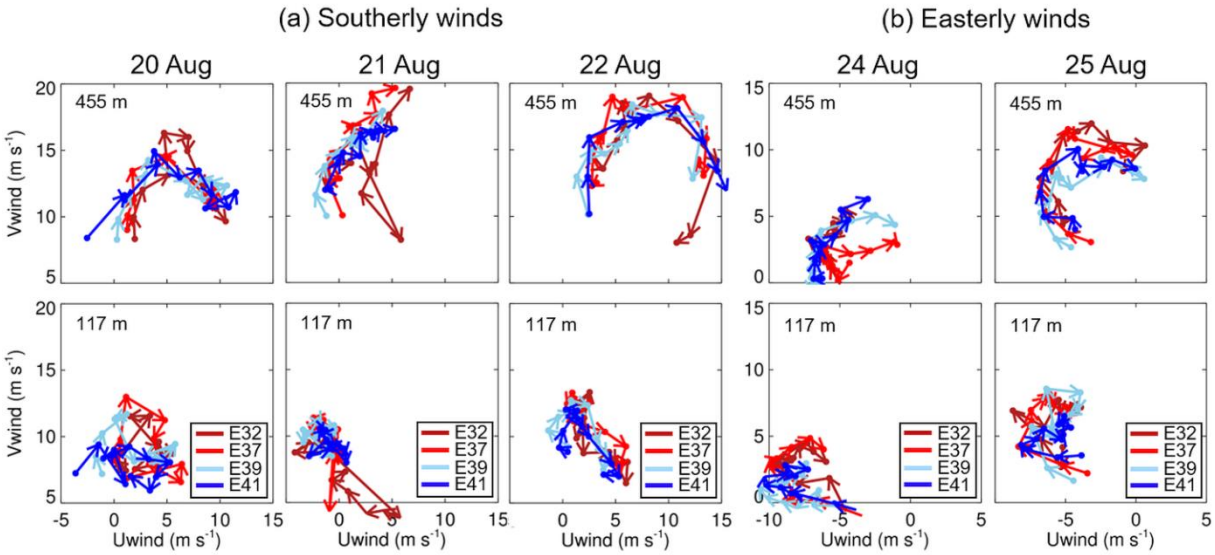

Fig. 13. Temporal hodographs for (a) southerly and (b) Easterly winds at 2 heights (117 and 455 m) illustrate clockwise rotation in time of winds at 4 SGP sites located at (west to east) 66-77 km and (north to south) 56-57 km.

Overall, the rotational amplitudes were small on most nights. If these small rotations had been observed at only one location, it might be easy to dismiss their validity as not significant, non-representative, or due to instrument uncertainty, but they were measured at all five sites. This smallness of the rotations means either that the late afternoon geostrophic departures were small, which we regard as unlikely, or that other factors or forces were important in the evolution of the LLJs besides pure IO physics. Such factors most likely include a significant role for height-dependent vertical mixing and/or processes contributing to a time-dependent geostrophic wind (e.g., Parish 1988).

Vertical hodographs. Vertical hodographs, shown for three times (0000, 0400, and 0600 UTC) in Fig. 14), reveal the vertical structure of the winds between 117 and 714 m AGL. In the late afternoon at 0000 UTC (top row), the strong mixing produced mostly small differences in the winds with height. Later in the evening at 0400 and 0600 UTC, the winds in the lower levels all blew from a similar direction, forming a linear hodograph configuration in which the wind speed increased with height but without significant change in direction. The

Accepted for publication in *Journal of Applied Meteorology and Climatology*. DOI 10.1175/JAMC-D-22-0128.1.

near-constancy of wind direction with height within the SBL below the jet nose has been previously noted in late summer and fall in southeast Colorado and Kansas (Pichugina and Banta 2010). Above this layer of uniform wind direction, the winds veered, giving the vertical hodograph a hooked appearance. This pattern was true for both the southerly and NE-flow nights. We note that Grachev et al. (2005) previously found evidence for Ekman turning in the very-stable, very-shallow boundary layer that persisted for many weeks in the Arctic, but we did not find such behavior within the overnight SBLs studied here.

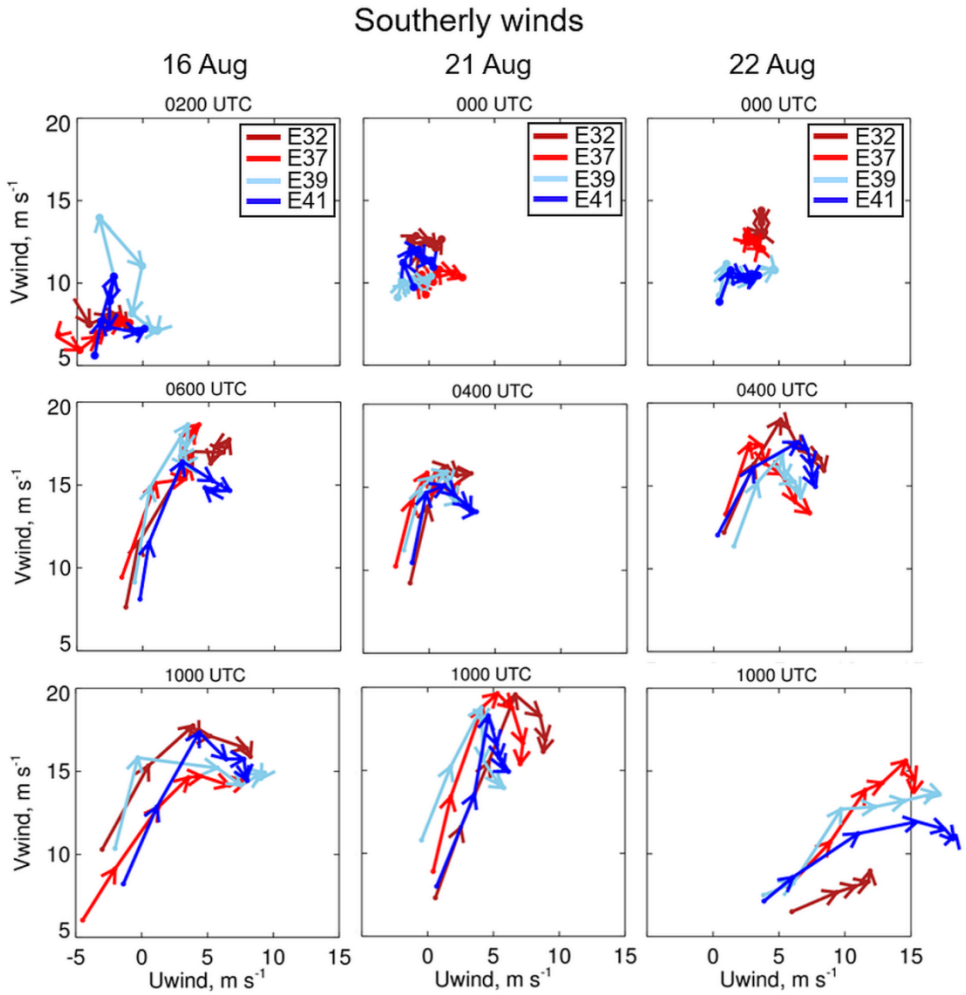

Fig. 14. Vertical "hooked" hodographs for southerly winds on 16, 21, and 22 August at 4 SGP sites. The first level represented in each hodograph was at 117 m, and the top level was 714 m AGL.

Other hodograph behavior. Temporal hodographs from weaker wind nights (e.g., Fig.15a) showed indications of veering, but not well organized and having less site-to-site coherence. Fig.15b shows an anomalous example of a temporal hodograph where the rotation turned counterclockwise with height at site E41 at 0400 UTC, then intensified and appeared at all the sites by 0600 UTC. [Although van de Wiel et al. (2010) found instances of such reverse

Accepted for publication in *Journal of Applied Meteorology and Climatology*. DOI 10.1175/JAMC-D-22-0128.1.

rotations on many nights by considering departures from an alternative reference wind profile, this was the only instance of counterclockwise rotation with the height that we found in the LAFE-period dataset]. Vertical hodographs also showed considerable variability among nights.

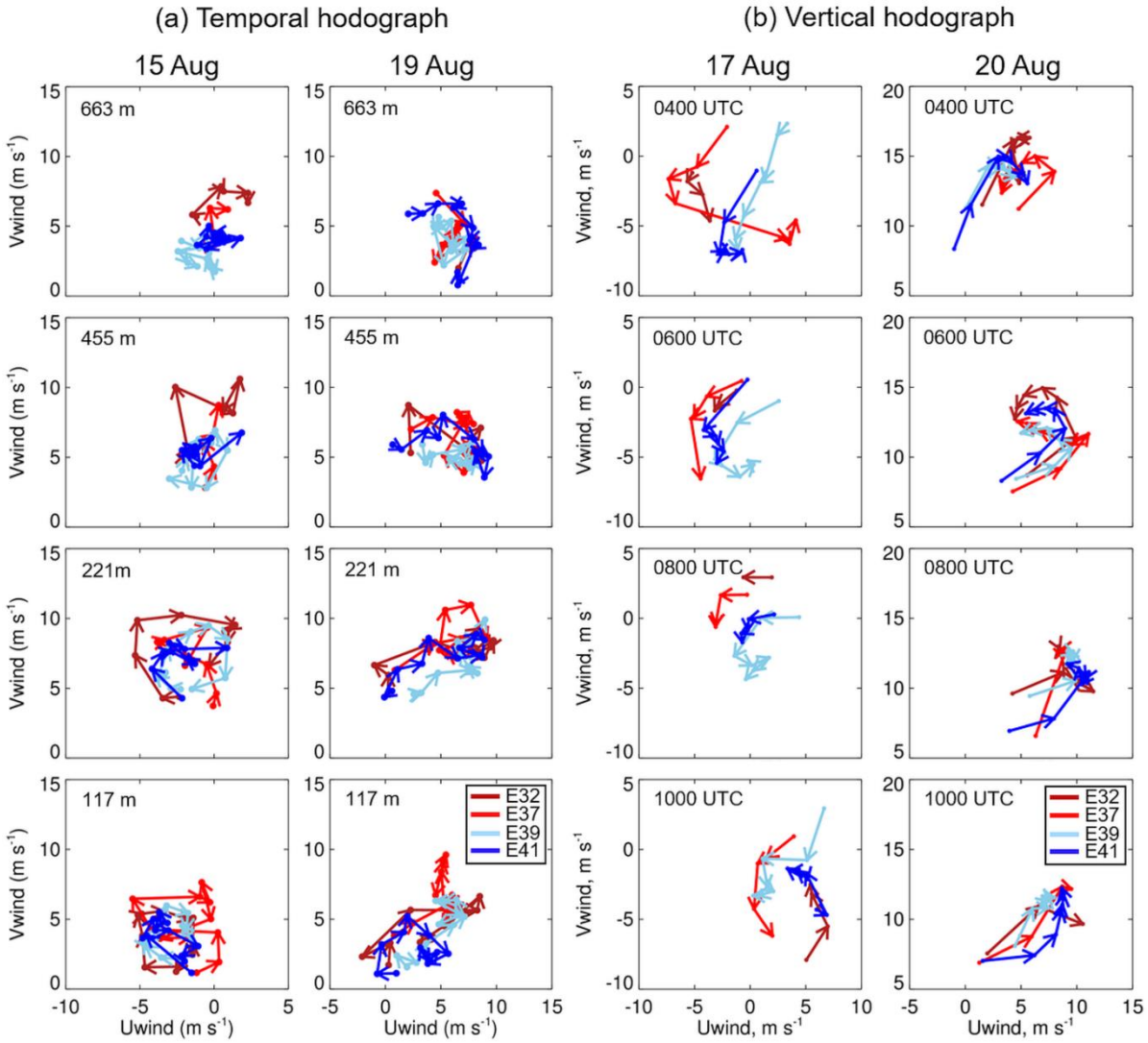

Fig. 15. Cases of unusual ("interesting") of (a) temporal and (b) vertical hodographs.

Accepted for publication in *Journal of Applied Meteorology and Climatology*. DOI 10.1175/JAMC-D-22-0128.1.

5. Conclusions

Doppler-lidar profiles of wind speed and direction were available at the central site during the intensive lidar deployment of LAFE, which was embedded in the SGP array of Doppler lidars. The availability of the six-year dataset from the five-site SGP array allowed the LAFE findings at the central site to be put into their spatial and temporal context. The layer-averaged nighttime winds showed a bimodal histogram in direction, with a predominant southerly peak and a secondary northeasterly peak that was usually much smaller. Southerly winds were stronger than the northeasterlies by more than 4 m s^{-1}on average. Geographic variations were noted: on southerly-wind nights, the winds blew strongest at the highest, westernmost sites by 2 m s^{-1}, whereas on the northeasterly-flow nights, the easternmost sites had the highest wind speeds by a similar margin.

In comparison with other summertime 2016-2021 months, August 2017, the period of deployment, showed an anomalously large number of post-cold-frontal days, characterized at night by a higher frequency of northerly through easterly LLJs than normal, a departure from the southerly winds and LLJs typical of summertime conditions in this region. Flow and LLJ properties could be compared for the same month, and the results echoed the results of the longer-term averages. Mean winds and LLJ speeds were stronger for the southerly flows than northeasterly flows by several m s^{-1}, reflecting a significantly higher frequency of winds stronger than 12 m s^{-1}. Under the southerly flow, speeds at the westernmost sites were ~1 m s^{-1} stronger than at the other sites.

The availability of frequent wind profiles at high vertical resolution allowed the construction of temporal and vertical hodographs over the study region. At levels within the SBL, the temporal hodographs showed a disorganized pattern, most likely due to the stronger mixing below the LLJ nose. Many nights where LLJs were observed featured the expected veering above the SBL. The total turning of the wind with time through the nights, however, was less than would be expected for a pure IO following an afternoon of strong convective heating through the Oklahoma ABL, which should generate a strong ageostrophic wind component at sunset. This indicates that mechanisms other than IO physics play a role in generating and maintaining the LLJ wind profile, such as turbulent mixing, thermal wind, or an evolving geostrophic wind.

Vertical hodographs of the wind profile in the SBL below the LLJ nose indicated dramatic increases in speed with height, but the direction was uniform, leading to a linear

Accepted for publication in *Journal of Applied Meteorology and Climatology*. DOI 10.1175/JAMC-D-22-0128.1.

hodograph in this layer. This provides evidence for significant vertical mixing of the winds in the SBL at night, but of course at intensities much less than daytime convective mixing. The turning of the wind with height was thus less than expected from Ekman theory, suggesting the influence of variable turbulent mixing with height. Above the SBL, veering with height above the linear trace within the SBL produced a hook-shaped hodograph. The similarity of the temporal and vertical hodographs from site to site reinforces their validity and shows that these were regional behaviors.

Acknowledgments

This study was conducted as part of the Land-Atmosphere Feedback Experiment (LAFE). This research was supported in part by NOAA cooperative agreements NA17OAR4320101 and 375 NA22OAR4320151, the U.S. the U.S. Department of Energy's Atmospheric System Research, an Office of Science Biological and Environmental Research program, under Grant No. DE-SC0020114, as part of the Atmospheric Radiation Measurement Program and Atmospheric System Research Program, and the NOAA Oceanic and Atmospheric Research Office of Weather and Air Quality, the NASA Water and Energy Cycle Program, the German Federal Ministry of Education and Research (BMBF), and the University of Hohenheim. We gratefully acknowledge the efforts of the ARM Southern Great Plains managers and PNLL staff for maintaining and operating that site both during this campaign and over the last three decades.

Data Availability Statement.

Datasets from scanning Doppler lidars at 5 SGP sites used during this study are openly available from the Atmospheric Radiation Measurement (ARM) Southern Great Plains (SGP) Archive at https://www.arm.gov/capabilities/observatories/sgp and are cited below:

Atmospheric Radiation Measurement (ARM) user facility. 2016. Doppler Lidar Horizontal Wind Profiles (DLPROFWIND4NEWS). 2021-06-01 to 2021-08-31, Southern Great Plains (SGP) Waukomis, OK (Extended) (E37). Compiled by T. Shippert, R. Newsom, and L. Riihimaki. ARM Data Center. Data set accessed at http://dx.doi.org/10.5439/1178582.

APPENDIXES

Appendix A. Temporal and vertical resolutions of data available from ULID during LAFE and the routine long-term SLID measurements.

	List of available 2D variables	Resolution time/vert.		Lowest height
Wind profiles				
Long-term SLID* lidars E32, E 37, E 39, E41 C1 (except LAFE period)	• wind speed • wind direction • u (eastward wind component) • v (northward wind component) • w (vertical wind component) • estimated errors of wind vectors	 10 min 15 min	 26 m 24 m	 90 m 90 m
ULID* lidar at C1 LAFE (13/08-6/09 2017)	• wind speed • wind direction	~1 min	21 m	10 m (good data from 53 m)
Turbulence profiles				
Long-term SLID lidars All 5 sites	• median SNR • w- median vertical velocity • variance of random noise in w • noise corrected w-variance • w-skewness and w-kurtosis	10 min	30 m	15 m (good data from 75 m)
ULID lidar at C1 LAFE (13/08-6/09 2017)	• Turbulence kinetic energy (TKE) • u-variance, v-variance, w-variance • u′w′ and v′w′ momentum fluxes	5 min	21 m	10 m (good data from 53 m)

*SLID- the ARM SGP Doppler lidar of long-term, baseline observations at 5 SGP sites;
**ULID-the Hohenheim Doppler lidar observations during LAFE

Table A. List of turbulence and wind flow variables obtained from SLIDs during the long-term (2016-2021) and from ULID during LAFE (Aug 2017) measurements along with a temporal and vertical resolution of profiles. The last column shows the first available height of the profile and (in parenthesis) the lowest height used to plot the paper figures.

Accepted for publication in *Journal of Applied Meteorology and Climatology*. DOI 10.1175/JAMC-D-22-0128.1.

Appendix B. Details of Fig.3

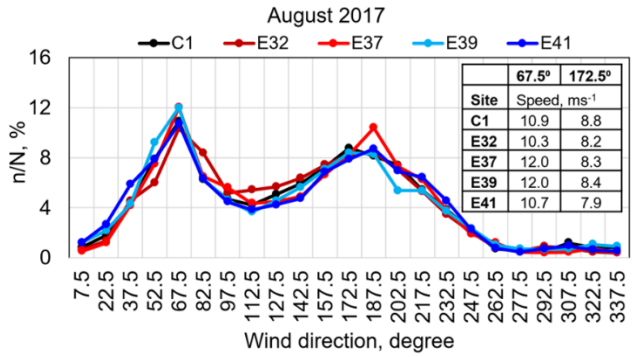

Fig. B1. Distributions of 0000-1400 UTC wind direction in the layer of 117-714 m at 5 SGP sites in August 2017 illustrates two prevalent wind directions: 67.5° and 172.5° . The embedded table shows the mean wind at each site for these direction-peaks.

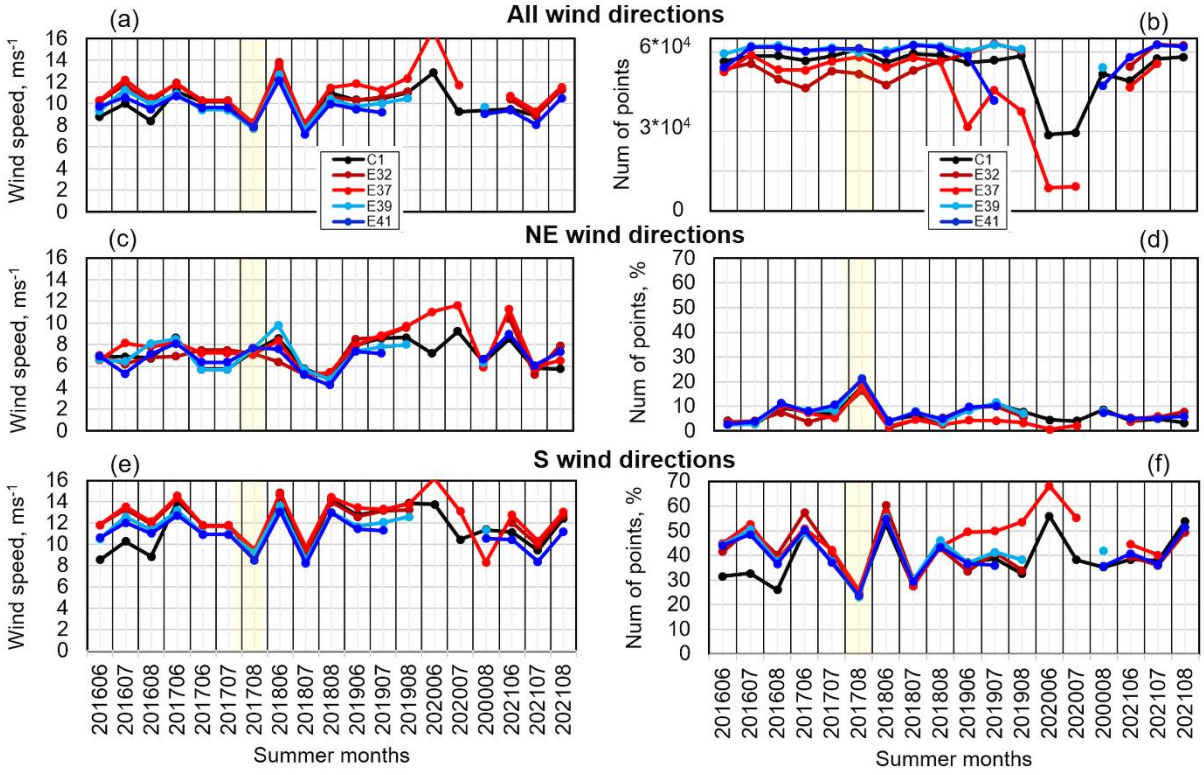

Fig. B2. (a) The monthly-mean wind speed and (b) the number of points used in Fig. 4 for the summer months of 2016-2021. Each site is shown by color according to the legend at the top panels. The bottom panels show (c, e) winds speed and (d, f) the number of points (%) for the NE (45° ± 22.5°) and S (180° ± 22.5°) sectors of wind direction. Missing data at some sites are due to instrument maintenance.

Wind speeds from the total sample were mostly 8-12 m s^{-1} (Fig. B2a). Each year, the strongest winds were southerly at all sites (Fig. B2c), whereas the north-easterly-component

Accepted for publication in *Journal of Applied Meteorology and Climatology*. DOI 10.1175/JAMC-D-22-0128.1.

sectors tended to be by 3-4 m s^{-1} weaker (Fig. B2e). The S-ly winds (Fig. B2d) were most frequent (25-60%) for all months and years. During the LAFE, the mean S-ly winds were weaker compared to other months and years (except July 2018), whereas the NE-ly-component winds were comparable to the other months. The frequency of NE-ly winds during Aug 2017 was larger (~22%) compared to other months.

Accepted for publication in *Journal of Applied Meteorology and Climatology*. DOI 10.1175/JAMC-D-22-0128.1.

Appendix C. Wind roses of (top) overnight (0000-1400) and (bottom) diurnal (0000-24000) winds at 117 m from lidar measurements at 5 SGP sites.

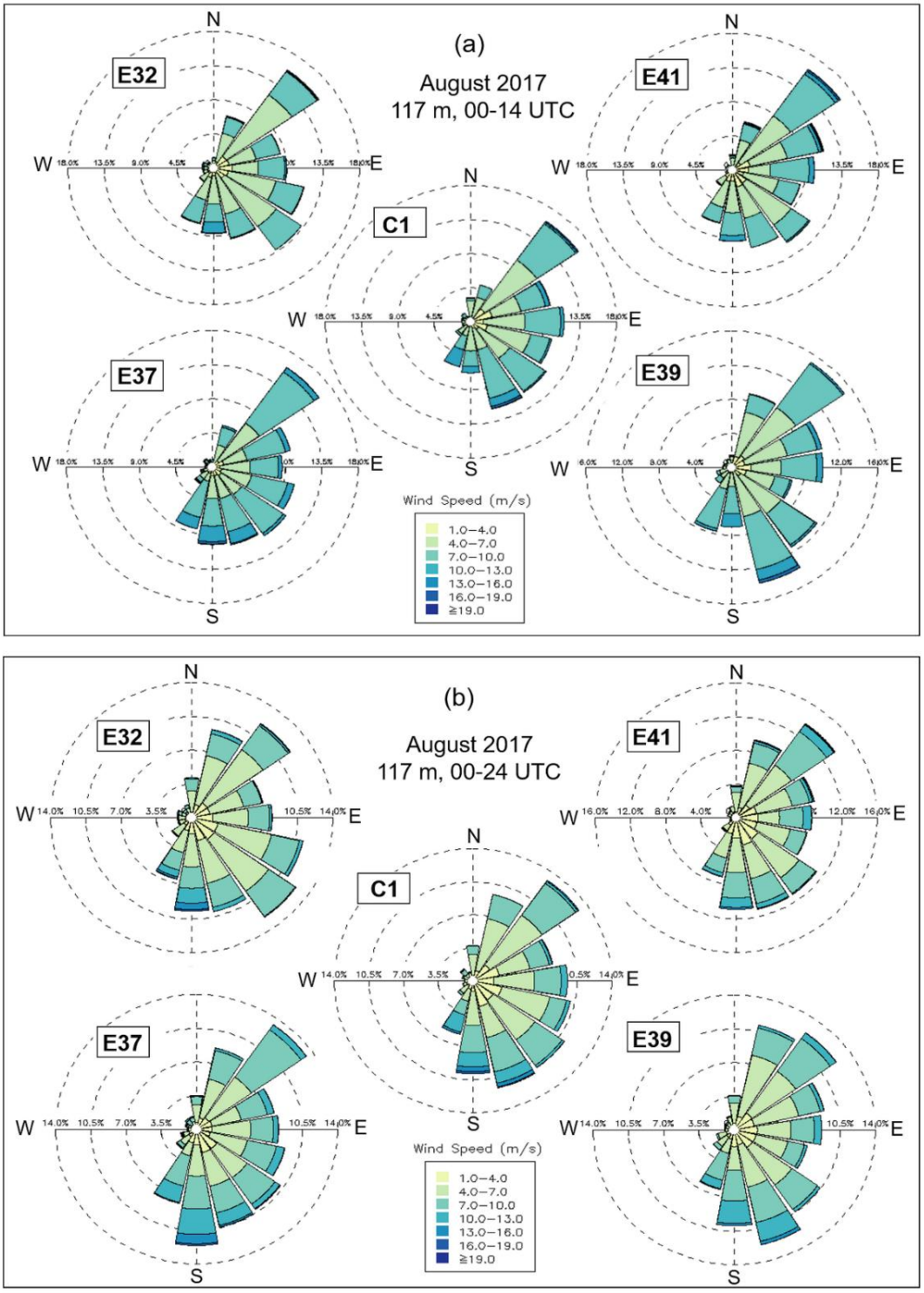

Fig. C. August 2017 wind roses of 117-m wind speed at the 5 SGP sites: (a) for 0000-1400 UTC and (b) for 0000-0024 UTC periods).

Accepted for publication in *Journal of Applied Meteorology and Climatology*. DOI 10.1175/JAMC-D-22-0128.1.

Appendix D. Frequency (%) of wind speed observed for different parts of a power curve of a "virtual "wind turbine

Site	**C1**		**E32**		**E37**		**E39**		**E41**	
Wind speed range	Count	%	Count	%	Count	***%***	Count	%	Count	%
	90 m									
0-25 m s $^{-1}$	2844	99	4319	99	4411	98	4455	99	4442	99
0-4 m s $^{-1}$	674	23	1083	25	918	20	1026	23	1262	28
4-12 m s $^{-1}$	2107	**74**	3165	**73**	3373	**76**	3366	**75**	3120	**70**
12-25 m s $^{-1}$	63	2	71	1	120	2	63	1	60	1
	117 m									
0-25 m s $^{-1}$	2884	98	4297	99	4388	99	4445	98	4438	99
0-4 m s $^{-1}$	621	21	951	22	885	20	923	20	1174	26
4-12 m s $^{-1}$	2127	**74**	3243	**75**	3316	**75**	3416	**76**	3175	**71**
12-25 m s $^{-1}$	96	3	103	2	187	4	106	2	89	2
	90-140 m									
0-25 m s $^{-1}$	8516	99	12786	99	13082	99	13333	99	13303	98
0-4 m s $^{-1}$	1837	21	2778	21	2617	20	2779	20	3393	25
4-12 m s $^{-1}$	6238	**73**	9485	**74**	9628	**73**	9887	**74**	9403	**70**
12-25 m s $^{-1}$	441	5	523	4	837	6	667	5	507	3

Table D. The total number (Count) and percentage (%) of 15-min at C1 and 10-min at E32-E41 wind speed data points in Aug 2017 at 90 and 117 m, and over a layer of 90-140 m is shown for different wind categories at each site. The categories are selected for a power curve of a "virtual "wind turbine and data are taken for the diurnal cycle of 0000-2400 UTC.

Accepted for publication in *Journal of Applied Meteorology and Climatology*. DOI 10.1175/JAMC-D-22-0128.1.

Appendix E. The stability classes based on the classification by the Monin-Obukhov length (L_{MO})

Nighttime BL conditions	Monin-Obukhov Length
very Stable (vS)	10 m $\leq L_{MO} \leq$ 50 m
Stable (S)	50 m $\leq L_{MO} \leq$ 200 m
near-neutral Stable (nnS)	200 m $\leq L_{MO} \leq$ 500 m
Neutral (N)	$\lvert L_{MO} \rvert \geq$500 m
near-neutral Unstable (nnU)	-500 m $\leq L_{MO} \leq$ -200 m

Table E. Classification of the nocturnal boundary layer stability by the Monin-Obukhov Length (L_{MO})

File generated with AMS Word template 2.0

Accepted for publication in *Journal of Applied Meteorology and Climatology*. DOI 10.1175/JAMC-D-22-0128.1.

REFERENCES

Balsley, B.B., R.G. Frehlich, M.L. Jensen, and Y. Meillier, 2006: High-resolution in situ profiling through the stable boundary layer: Examination of the SBL top in terms of minimum shear, maximum stratification, and turbulence decrease. *J. Atmos. Sci.*, **63**, 1291-1307, https://doi.org/10.1175/JAS3671.1.

Banta, R.M., C. J. Senff, A.B. White , M. Trainer, R.T. McNider, R.J. Valente, S.D. Mayor, R.J. Alvarez, R.M. Hardesty, D.D. Parrish, and F.C. Fehsenfeld, 1998: Daytime buildup and nighttime transport of urban ozone in the boundary layer during a stagnation episode. *J. Geophys. Res.*, **103**, 22,519-22,544, https://doi.org/10.1029/98JD01020.

Banta, R.M., R.K. Newsom, J.K. Lundquist, Y.L. Pichugina, R.L. Coulter, and L. Mahrt, 2002: Nocturnal low-level jet characteristics over Kansas during CASES-99. *Boundary-Layer Meteorol*., **105**: 221–252.

Banta, R.M., Y.L. Pichugina, and R.K. Newsom, 2003: Relationship between Low-Level Jet Properties and Turbulence Kinetic Energy in the Nocturnal Stable Boundary Layer. *J. Atmos. Sci.,* **60**, 2549–2555, https://doi.org/10.1175/1520-0469(2003).

Banta, R.M., C. J. Senff, J. Nielsen-Gammon, L. S. Darby, T. B. Ryerson, R. J. Alvarez, S. P. Sandberg, E. J. Williams, and M. Trainer, 2005: A bad air day in Houston. *Bull. Amer. Meteor. Soc.*, **86**, 657–669, https://doi.org/10.1175/BAMS-86-5-657.

Banta, R.M., Y.L. Pichugina, and W.A. Brewer, 2006: Turbulent Velocity-Variance Profiles in the Stable Boundary Layer Generated by a Nocturnal Low-Level Jet. *J. Atmos. Sci.*, **63**, 2700–2719, https://doi.org/10.1175/JAS3776.1.

Banta, R. M., Mahrt, L., Vickers, D., Sun, J., Balsley, B. B., Pichugina, Y. L., & Williams, E. L., 2007: The very stable boundary layer on nights with weak low-level jets. *J. Atmos. Sci.*, ***64***(9), 3068-3090, http://doi.org/10.1175/JAS4002.1.

Banta RM, Pichugina YL, Kelley ND, Hardesty RM, Brewer WA, 2013. Wind energy meteorology: Insight into wind properties in the turbine-rotor layer of the atmosphere from high resolution Doppler lidar. *Bulletin of the American Meteorological Society*, **94**, 6, 883-902, http://dx.doi.org/10.1175/BAMS-D-11-00057.1.

Banta, R.M., Y.L. Pichugina, W.A. Brewer, E.P. James, J.B. Olson, S.G. Benjamin, J.R. Carley, L. Bianco, I.V. Djalalova, J.M. Wilczak, M.C. Marquis, J. Cline, and R.M.

Accepted for publication in *Journal of Applied Meteorology and Climatology*. DOI 10.1175/JAMC-D-22-0128.1.

Hardesty, 2018: Evaluating and improving NWP forecasts for the future: How the needs of offshore wind energy can point the way. *Bull. Amer. Meteor. Soc.*, **99**, 1155-1176, doi.org/10.1175/BAMS-D-16-0310.1.

Blackadar, A. K., 1957: Boundary layer wind maxima and their significance for the growth of nocturnal inversions. *Bulletin of the American Meteorological Society*, **38**, 283–290, https://doi.org/10.1175/1520-0477-38.5.283.

Bonin, T. A., Choukulkar, A., Brewer, W. A., Sandberg, S. P., Weickmann, A. M., Pichugina, Y. L., Banta, R. M., Oncley, S. P., and Wolfe, D. E., 2017: Evaluation of turbulence measurement techniques from a single Doppler lidar. *Atmos. Meas. Tech.*, **10**, 3021–3039, https://doi.org/10.5194/amt-10-3021-2017.

Bonin, T.A., P.M. Klein, and P.B. Chilson, 2020: Contrasting characteristics and evolution of southerly low-level jets during different boundary-layer regimes. *Bound.-Layer Meteor.*, **174**, 179–202, https://doi.org/10.1007/s10546-019-00481-0.

Bonner, W.D., 1968: Climatology of the low-level jet. *Mon. Wea. Rev.*, 96, 833–850, https://doi.org/10.1175/1520-0493(1968)096,0833:COTLLJ.2.0.CO;2.

Carroll, B. J., B. B. Demoz, and R. Delgado, 2019: An overview of low-level jet winds and corresponding mixed layer depths during PECAN. *J. Geophys. Res.*, **124**, 9141–9160, https://doi.org/10.1029/2019JD030658.

Carroll, B.J., B.B. Demoz, D.D. Turner, and R. Delgado, 2021: Lidar observations of a mesoscale moisture transport event impacting convection and comparison to rapid refresh model analysis. *Mon. Wea. Rev.*, **149**, 463-477, https://doi.org/10.1175/MWR-D-20-0151.1.

Fedorovich, E., J.A. Gibbs, and A. Shapiro, 2017: Numerical study of nocturnal low-level jets over gently sloping terrain. *J. Atmos. Sci.*, **74**, 2813–2834, https://doi.org/10.1175/JAS-D-17-0013.1.

GE Energy: 1.5MW wind turbine, 2009. Available online at https://en.wind-turbine-models.com/turbines/655-ge-general-electric-ge-1.5sle

Gebauer, J. G., E. Fedorovich, and A. Shapiro, 2017: A 1D theoretical analysis of northerly low-level jets over the Great Plains. *J. Atmos. Sci.*, **74**, 3419–3431, https://doi.org/10.1175/JAS-D-16-0333.1.

Accepted for publication in *Journal of Applied Meteorology and Climatology*. DOI 10.1175/JAMC-D-22-0128.1.

——, A. Shapiro, E. Fedorovich, and P. Klein, 2018: Convection initiation caused by heterogeneous low-level jets over the Great Plains. *Mon. Wea. Rev.*, **146**, 2615–2637, https://doi.org/10.1175/MWR-D-18-0002.1.

Grachev, A.A., Fairall, C.W., Persson, P.O.G., and Coauthors, 2005: Stable Boundary-Layer Scaling Regimes: The Sheba Data. *Boundary-Layer Meteorol* **116,** 201–235, https://doi.org/10.1007/s10546-004-2729-0.

Higgins, R. W., Y. Yao, E. S. Yarosh, J. E. Janowiak, and K. C. Mo, 1997: Influence of the Great Plains low-level jet on summertime precipitation and moisture transport over the central United States. *J. Climate,* **10**, 481–507, https://doi.org/10.1175/1520-0442(1997)010,0481:IOTGPL.2.0.CO;2.

Holton, J.R., 1967: The diurnal boundary layer wind oscillation above sloping terrain. *Tellus*, **19**, 199–205, https://doi.org/10.1111/j.2153-3490.1967.tb01473.x.

Kelley, N, M. Shirazi, D. Jager, S. Wilde, J. Adams, and M. Buhl, 2004: Lamar Low-Level Jet Project Interim Report NREL/TP-500-34593.

Klein, P. M., X.-M. Hu, and M. Xue, 2014: Impacts of mixing processes in nocturnal atmospheric boundary layer on urban ozone concentrations. *Bound.-Layer Meteor.*, **150**, 107–130, https://doi.org/10.1007/s10546-013-9864-4.

Klein P, Bonin TA, Newman JF, Turner DD, Chilson PB, Wainwright CE, Blumberg WG, Mishra S, Carney M, Jacobsen EP, Wharton S, Newsom RK (2015) LABLE: amulti-institutional, student-led, atmospheric boundary-layer experiment. Bull Am Meteorol Soc. doi: 10.1175/BAMS-D-13-00267.

Lundquist, J.K., 2003: Intermittent and elliptical inertial oscillations in the atmospheric boundary layer. *J. Atmos. Sci.*, **60**, 2661-2673.

Mahrt, L. Stratified atmospheric boundary layers and breakdown of models. 1998: *Theoret. Comput. Fluid Dynamics*, **11**, 263–279, https://doi.org/10.1007/s001620050093.

Mahrt, L., R.C. Heald, D.H. Lenschow, B.B. Stankov, and I. Troen, 1979: An observational study of the structure of the nocturnal boundary layer. *Bound.-Layer Meteor.*, **17**, 247–264.

Accepted for publication in *Journal of Applied Meteorology and Climatology*. DOI 10.1175/JAMC-D-22-0128.1.

Meyers, Tilden, Lee, Temple R, Baker, C Bruce, Buban, Michael, & Dumas, Edward. NOAA Air Resources Laboratory Atmospheric Turbulence and Diffusion Division Contribution to LAFE Field Campaign Report. DOE/SC-ARM-18-011. United States.

Means, L.L., 1954: A study of the mean southerly wind maximum in low levels associated with a period of summer precipitation in the Middle West. *Bull. Amer. Meteor. Soc.*, **35**, 166–170, DOI:10.1175/1520-0477-35.4.166.

Mirocha, J.D., M.D. Simpson, J.D. Fast, L.K. Berg, and R.L. Baskett, 2016: Investigation of boundary-layer wind predictions during nocturnal low-level jet events using the Weather Research and Forecasting Model. *Wind Energy*, **19**, 739–762, https://doi.org/10.1002/we.1862.

Mitchell, M.J., R.W. Arritt, and K. Labas, 1995: A climatology of warm season Great Plains low-level jet using wind profiler observations. *Wea. Forecasting*, **10**, 576–591, DOI:10.1175/1520-0434(1995)010<0576:ACOTWS>2.0.CO;2.

Mo, K., J.N. Paegle, and J. Paegle, 1995: Physical mechanisms of the 1993 floods. *J. Atmos. Sci.*,**52**, 879–895.

Newsom, R.K. and Krishnamurthy R, 2020: Doppler Lidar (DL) Instrument Handbook, DOE/SC-ARM-TR-101.

Ohya, Y., R. Nakamura, and T. Uchida, 2008: Intermittent bursting of turbulence in a stable boundary layer with low-level jet. *Bound.-Layer Meteor.*, **126**, 349–363, http://dx.doi.org/10.1007/s10546-007-9245-y.

Parish, T. R., A. R. Rodi, and R. D. Clark, 1988: A case study of the summertime Great Plains low level jet. *Mon. Wea. Rev.*, **116**, 94–105, https://doi.org/10.1175/1520-0493(1988)116<0094:ACSOTS>2.0.CO;2.

——, and L. D. Oolman, 2010: On the role of sloping terrain in the forcing of the Great Plains low-level jet. *J. Atmos. Sci.*, **67**, 2690–2699, https://doi.org/10.1175/2010JAS3368.1.

——, and R. D. Clark, 2017: On the initiation of the 20 June 2015 Great Plains low-level jet. *J. Appl. Meteor. Climatol.*, **56**, 1883–1895, https://doi.org/10.1175/JAMC-D-16-0187.1.

Accepted for publication in *Journal of Applied Meteorology and Climatology*. DOI 10.1175/JAMC-D-22-0128.1.

Phillips, T. J., & Klein, S. A. (2014). Land-atmosphere coupling manifested in warm-season observations on the U.S. Southern Great Plains. *Journal of Geophysical Research: Atmospheres*, **119**, 509–528, https://doi.org/10.1002/2013JD020492.

Pichugina, Y. L., Banta R.M., Kelley N. D., Jonkman B. J., Tucker S. C., Newsom R. K., Brewer W. A.., 2008: Horizontal-velocity and variance measurements in the stable boundary layer using Doppler lidar: sensitivity to averaging procedures. *Journal of Atmospheric and Oceanic Technology* **25**: 1307–1327, https://doi.org/10.1175/2008JTECHA988.1.

Pichugina, Y. L., Banta R. M., 2010: Stable boundary-layer depth from high-resolution measurements of the mean wind profile. J. Appl. Meteor. Climatol. 2010; 49: 20–35, https://doi.org/10.1175/2009JAMC2168.1.

Pichugina, Y.L., R.M. Banta, and Coauthors, 2019: Spatial variability of winds and HRRR-NCEP model error statistics at three Doppler-lidar sites in the wind-energy generation region of the Columbia River Basin. *J. Appl. Meteor. Climatol.*, **58**, 1633-1656. doi.org/10.1175/JAMC-D-11-040.1.

Pitchford, K. L., and J. London, 1962: The low-level jet as related to nocturnal thunderstorms over Midwest United States. *J. Appl. Meteor.*, **1**, 43–47, https://doi.org/10.1175/15200450(1962)001,0043:TLLJAR.2.0.CO;2.

Poulos, G. S., W. Blumen, D. C. Fritts, J. K. Lundquist, J. Sun, S. P. Burns, Carmen Nappo, R. Banta, R. Newsom, J. Cuxart, E. Terradellas, B. Balsley, and M. Jensen, 2002: CASES-99: A comprehensive investigation of the stable nocturnal boundary layer. *Bulletin of the American Meteorological Society*, **83**(4):555-581, https://doi.org/10.1175/1520-0477(2002)083<0555:CACIOT>2.3.CO;2 .

Pu, B., and R.E. Dickinson, 2014: Diurnal spatial variability of Great Plains summer precipitation related to the dynamics of the low-level jet. *J. Atmos. Sci.*, **71**, 1807–1817, https://doi.org/10.1175/JAS-D-13-0243.1.

Sathe, A., Mann, J., Vasiljevic, N., & Lea, G. (2015). A six-beam method to measure turbulence statistics using ground-based wind lidars. *Atmospheric Measurement Techniques*, **8**(2), 729–740, https://doi.org/10.5194/amt-8-729-2015.

Accepted for publication in *Journal of Applied Meteorology and Climatology*. DOI 10.1175/JAMC-D-22-0128.1.

Shapiro, A., and E. Fedorovich, 2009: Nocturnal low-level jet of a shallow slope. Acta Geophys., **7**, 950–980, https://doi.org/10.2478/s11600-009-0026-5.

——, and ——, 2010: Analytical description of a nocturnal low-level jet. *Quart. J. Roy. Meteor. Soc.*, **136**, 1255–1262. https://doi.org/10.1002/qj.628.

——, ——, and S. Rahimi, 2016: A unified theory for the Great Plains low-level jet. *J. Atmos. Sci.*, **73**, 3037–3056, https://doi.org/10.1175/JAS-D-15-0307.1.

Smith, E.N., J. Gibbs, E. Fedorovich, and P. M. Klein, 2018: WRF Model study of the Great Plains low-level jet: Effects of grid spacing and boundary layer parameterization. *J. Appl. Meteor. Climatol.*, **57**, 2375–2397, https://doi.org/10.1175/JAMC-D-17-0361.1.

Smith, E.N., J. G. Gebauer, P. M. Klein, E. Fedorovich, and J. A. Gibbs, 2019: The Great Plains low-level jet during PECAN: Observed and simulated characteristics. *Mon. Wea. Rev.*, **147**, 1845–1869, https://doi.org/10.1175/MWR-D-18-0293.1.

Song, J., K. Liao, R.L. Coulter, and B.M. Lesht, 2005: Climatology of the low-level jet at the Southern Great Plains Atmospheric Boundary Layer Experiments site. *J. Appl. Meteor.*, 44, 1593–1606, https://doi.org/10.1175/JAM2294.1.

Storm, B., J. Dudhia, S. Basu, A. Swift, and I. Giammanco, 2009: Evaluation of the Weather Research and Forecasting Model on forecasting low-level jets: Implications for wind energy. *Wind Energy*, **12**, 81–90. https://doi.org/10.1002/we.288.

Turner D. D., V. Wulfmeyer, A. Behrendt, T. A. Bonin, A. Choukulkar, R. K. Newsom, W. A. Brewer, D. R. Cook, 2017, Response of the Land-Atmosphere System Over North-Central Oklahoma During the 2017 Eclipse." Geophysical Research Letters 45(3): 1668-1675,, https://doi.org/10.1002/2017GL076908

Van de Wiel, B. J. H., A.F. Moene, G.J. Steeneveld, P. Baas, F.C. Bosveld, and A.A.M. Holtslag, 2010: A conceptual view on inertial oscillations and nocturnal low-level jets. *J. Atmos. Sci.*, **67**, 2679–2689, doi:10.1175/2010JAS3289.1.

Vanderwende, B.J., J.K. Lundquist, M.E. Rhodes, E.S. Takle, and S.L. Irvin, 2015: Observing and simulating the summertime low-level jet in central Iowa. *Mon. Wea. Rev.*, **143**, 2319–2336, https://doi.org/10.1175/MWR-D-14-00325.1.

Accepted for publication in *Journal of Applied Meteorology and Climatology*. DOI 10.1175/JAMC-D-22-0128.1.

Vogelezang, D.H.P., Holtslag, A.A.M, 1996: Evaluation and model impacts of alternative boundary-layer height formulations. *Boundary-Layer Meteorol* **81,** 245–269, https://doi.org/10.1007/BF02430331.

Werth, D., R. Kurzeja, N.L. Dias, G. Zhang, H. Duarte, M. Fischer, M. Parker, and M. Leclerc, 2011: The simulation of the southern Great Plains nocturnal boundary layer and the low-level jet with a high-resolution mesoscale atmospheric model. *J. Appl. Meteor. Climatol.*, **50**, 1497–1513, https://doi.org/10.1175/2011JAMC2272.1.

Whiteman, C.D., X. Bian, and S. Zhong, 1997: Low-level jet climatology from enhanced rawinsonde observations at a site in the Southern Great Plains. *J. Appl. Meteor.*, **36**, 1363–1375, https://doi.org/10.1175/1520-0450(1997)036,1363:LLJCFE.2.0.CO;2.

Wulfmeyer, V., D.D. Turner, B. Baker, R. Banta, A. Behrendt, T. Bonin, W.A. Brewer, M. Buban, A. Choukulkar, E Dumas, RM Hardesty, T Heus, J Ingwersen, D Lange, TR Lee, S Metzendorf, SK Muppa, T. Meyers, R Newsom, M Osman, S Raasch, J Santanello, C Senff, F Späth, T Wagner, T Weckwerth, 2018: "A new research approach for observing and characterizing land-atmosphere feedback." *Bull. Amer. Meteor. Soc.*, **99**(8), 1639-1667, http://dx.doi.org/10.1175/BAMS-D-17-0009.1.

Zhong, S., J. Fast, and X. Bian, 1996: A case study of the Great Plains low-level jet using wind profiler network data and a high-resolution mesoscale model. *Mon. Wea. Rev.*, **124**, 785–806, https://doi.org/10.1175/1520-0493(1996)124,0785:ACSOTG.2.0.CO;2.

Accepted for publication in *Journal of Applied Meteorology and Climatology*. DOI 10.1175/JAMC-D-22-0128.1.